ACS OMEGA

http://pubs.acs.org/journal/acsodf

Article

New Rare Earth-Doped Bilayered Perovskite Oxide Photocatalysts $Sr_2La_{0.5}R_{0.5}FeMnO_7$ (R = La, Nd, Sm, Gd, Dy) for the Degradation of Highly Toxic Methylene Blue Dye in Wastewater under Visible Light: Structural, Optical, and Magnetic Properties

Irfan Qadir, Sumit Singh, Shikha Sharma, Ujwal Manhas, Amit Kumar Atri, and Devinder Singh*

Cite This: *ACS Omega* 2023, 8, 2010−2026

Read Online

ACCESS | Metrics & More | Article Recommendations

ABSTRACT: This paper presents the rare earth doping effect on the structural, optical, and magnetic properties of bilayered Ruddlesden−Popper oxides $Sr_2La_{0.5}R_{0.5}FeMnO_7$ (R = La, Nd, Sm, Gd, Dy). Moreover, we are reporting for the first time a new rare earth-doped bilayered perovskite oxide series for the highly toxic methylene blue dye degradation in wastewater under visible light. Structural analysis of the PXRD data using the Rietveld refinements confirms the formation of the phases in tetragonal symmetry with the *I*4/*mmm* space group. The unit cell lattice parameters (*a* & *c*) and the cell volume (*V*) decrease monotonically from La- to Dy-doped samples owing to the decrease in the lanthanide ionic radii. The X-ray photoelectron spectroscopy analysis indicates the existence of the Mn ions in the mixed valence state. The DRS study shows that the energy band gap value decreases on moving from La to Gd substitution; however, it further increases for the Dy-doped sample. The magnetic measurements reveal that all the phases exhibit dominant anti-ferromagnetic interactions with Neel temperature (T_N) observed at 150, 147, 138, 113, and 117 K for La-, Nd-, Sm-, Gd-, and Dy-substituted phases, respectively. However, the presence of an unsaturated hysteresis loop observed in the isothermal magnetic field (*H*) vs magnetization (*M*) plot also indicates the existence of weak ferromagnetic interactions. The investigation of the photocatalytic activity of the synthesized samples was done by carrying out photo-oxidative degradation of methylene blue (MB) dye pollutants. The results show that the photodegradation enhances by doping with heavier rare earth ions with the exception of the Dy-doped sample. The Gd-doped catalyst shows the maximum degradation efficiency of 99.03% in 50 min under visible light irradiation. The scavenging experiments confirmed that the $^{\cdot}OH$ was the main/dominant oxidizing agent involved in the degradation of the MB dye.

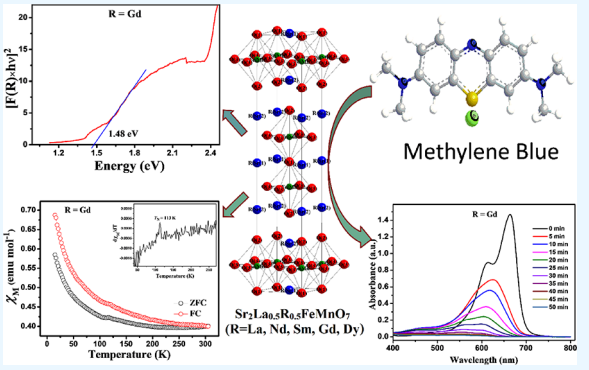

1. INTRODUCTION

The perovskite manganate oxides with various combinations of transition and rare earth metals have widely been studied owing to their diverse physical properties like magneto-resistance, multiferroic properties, exchange bias (EB), magnetic information storage, magnetic field sensors,[1−5] etc. However, over the years, a similar interesting behavior and significant magnetoresistance effect have also been observed in quasi two-dimensional layered perovskite Ruddlesden−Popper (RP) manganite oxides.[6−10] The RP oxides are given by the general formula $A_{n+1}B_nO_{3n+1}$. Here, *n* gives the number of perovskite layers sandwiched between the AO rock salt layers in a unit cell, B is a transition metal ion, and A is a rare earth or alkaline earth or alkali metal ion. The RP phases mostly crystallize in the orthorhombic or tetragonal unit cell with the *Fmmm* or *I*4/*mmm* space group, respectively. The quasi dimensionality in the RP oxides originates from the presence of nonmagnetic AO layers separating the perovskite blocks along the crystallographic *c* axis.

The $Ln_{2-x}Sr_{1+x}Mn_2O_7$ ($0 \le x \le 1$) system could be seen as the *n* = 2 member of the RP oxides. It has been observed that the structural and magneto transport properties of such *n* = 2 phases are sensitive to both the Ln/Sr ratio and the nature of the Ln ion.[11] The $La_{2-x}Sr_{1+x}Mn_2O_7$ phase shows magneto-resistance and exhibits metal−insulator transition at its ferromagnetic ordering temperature (T_c).[12,13] $Nd_{1+x}Sr_{2-x}Mn_2O_7$ shows a significant magnetoresistance effect

Received: August 14, 2022
Accepted: December 20, 2022
Published: January 4, 2023

despite having antiferromagnetic coupling.[14,15] Substitution by smaller lanthanide ions such as Ho and Y results in reduction in the symmetry from the $I4/mmm$ to $P4_2/mmm$ space group.[16] For $LaSr_2Mn_2O_7$, magnetic coupling is ferromagnetic within the constituent single MnO_2 layer; however, it shows A-type antiferromagnetic ordering ($T_N \approx 220$ K) between the respective single MnO_2 layers within the bilayer unit.[17] The $n = 1$ $La_{1-x}Sr_{1+x}MnO_4$ RP phase shows a decrease in T_N with the increase in x, and spin-glass behavior appears for $x \geq 0.2$, owing to the competing antiferromagnetic superexchange and ferromagnetic double-exchange interactions.[18]

The substitution of other transition metal ions in the Mn ion site leads to interesting property changes in the RP manganites. Sharma et al.[19] showed that $LaSr_2MnFeO_7$ is oxygen deficient and the Mn ion exists in the mixed valence state. The Cr doping in $LaSr_2Mn_2O_7$ results in the disappearance of insulator−metal transition, and both the AFM Neel temperature and charge-ordered temperature shift to lower values with the increase in Cr substitution.[20] In the $LnSr_2MnFeO_7$ system, the unit cell parameters a and c decrease, while the Weiss constant (θ) increases with the decrease in the lanthanide radii, although all the Ln substituted phases exhibit antiferromagnetic ordering. $Sr_3Mn_{2-x}Fe_xO_{7-\delta}$ ($0.10 \leq x \leq 0.5$) phases show spin-glass transition but only for the $x = 0.5$ phase as evident from the maximum at 12 K shown in the ZFC susceptibility curve.[21] The $SrLaFe_{0.25+x}Mn_{0.25}Co_{0.5-x}O_4$ phases reveal two transitions in the DC magnetization variation with temperature. The short-range antiferromagnetic ordering is observed at 297 and 318 K, while the frozen magnetic behavior is obtained at 23 and 43 K for $x = 0$ and 0.25 phases, respectively.[22]

A number of heterojunction catalysts have been recently reported for the removal of water hyacinth and pharmaceutical pollutants.[23−28] The applicability of photocatalytic degradation of organic dye pollutants in wastewater management by semiconductors like TiO_2, ZnO, and SnO_2 is limited as they absorb only a small part of the solar spectrum. Thus, the development of photodegradation of dye by utilizing visible light has recently become an important topic of research. The RP-oxides in general being good semiconducting materials can absorb well in the visible light region, resulting in the excitation of the valence band electrons to the conduction band. The electron−hole pairs thus formed can further generate free radicals, which will then degrade the organic pollutants since they are strong oxidizing agents of organic materials.[29,30] Ca-doped lanthanum manganite nanowires display sufficient visible-light photocatalysis for the water treatment of methylene blue (MB) dye pollutant and show a photodegradation efficiency of 73% for 7 ppm MB dye degradation after 360 min illumination.[31] The photocatalytic hydrogen production significantly improves when the Sr_2TiO_4 system is doped with La and Fe.[32] In the case of the $Sr_{3.2-x}Ca_xLa_{0.8}Fe_{1.5}O_{10-\delta}$ system, the methylene blue (MB) photodegradation enhances with the increase in Ca substitution and the complete degradation occurs for $x = 0.8$ in 150 min.[33] Guo et al.[34] observed that with the increase in Sr content, the degradation of rhodamine B by the $La_{1-x}Sr_xMnO_3$ catalyst enhances under strong acidic conditions.

Though a lot of work has been done on $n = 1$ RP phases, the reports on structural, magnetic and especially photocatalytic properties pertaining to $n = 2$ members are limited. Moreover, oxygen deficiency in RP phases has a significant effect on magnetic and photocatalytic properties. In view of this, a new oxygen-deficient $n = 2$ RP series $Sr_2La_{0.5}R_{0.5}FeMnO_7$ (R = La, Nd, Sm, Gd, Dy) has been synthesized by the sol−gel method, and its structural and magnetic properties have been investigated. Further, we checked the applicability of the synthesized phases for their photocatalytic activity in the degradation of organic dye pollutants.

2. EXPERIMENTAL SECTION

The synthesis of the $Sr_2La_{0.5}R_{0.5}FeMnO_7$ (R = La, Nd, Sm, Gd, Dy) was done *via* the sol−gel-based Pechini method. The stoichiometric amounts of analytical grade La_2O_3 (99.9% Sigma Aldrich), Nd_2O_3 (99.9% Loba Chemie), Sm_2O_3 (99.9% Loba Chemie), Gd_2O_3 (99.9% Loba Chemie), Dy_2O_3 (99.9% Loba Chemie), $Sr(NO_3)_2$ (99.0% Alfa Aesar), $Mn(CH_3COO)_2{\cdot}4H_2O$ (99.9% Sigma Aldrich), $Fe(NO_3)_3{\cdot}9H_2O$ (98 + % Alfa Aesar), $(CH_2OH)_2$ (Loba Chemie), and $HOC(CO_2H)(CH_2CO_2H)_2$ (99.5 + % Alfa Aesar) were used as precursor materials. Before usage, the R_2O_3 (La, Nd, Sm, Gd, and Dy) was heated at 1000 °C for 6 h to remove the moisture and other gases. The rare earth oxides were converted into corresponding nitrates by dissolving them in a 3 N HNO_3 solution. The rare earth nitrate solution was then mixed with the metal nitrate solution prepared by using the stoichiometric amounts of $Fe(NO_3)_3{\cdot}9H_2O$, $Sr(NO_3)_2$, and $Mn(CH_3COO)_2$ in a triple distilled water, and the resulting solution was kept on a magnetic stirrer for 1 h. The solution of citric acid prepared separately by dissolving it in water in the 2:1 molar ratio w.r.t the total metal cations were mixed with the metal nitrate solution and then stirred further for 1 h. As a result, the formation of a chelate between the citric acid and mixed cations takes place. Finally, the reaction mixture solution was added with the ethylene glycol taken in a 4:1 molar ratio w.r.t the total metal cations, and the resulting solution was again continuously stirred for 1 h. This aids in the cross-linkings between the chelates to create a polymeric precursor *via* esterification. The resulting final solution was transferred in a beaker (3000 mL) and then placed on a hot plate till the formation of a gel. The gel was finally heated in an oven where the combustion takes place at ∼260 °C. The powder samples thus obtained from combustion were sintered for 6 h at 800 °C in a muffle furnace, and after cooling, they were ground into a fine powder, using a mortar and pestle. The powdered samples are further compressed into pellets by using a hydraulic press and then calcined at 1350 °C for 40 h using an electric furnace with three intermediate pelletizing and grinding. Finally, the pellets were let to cool down till room temperature and then ground into fine powder for further investigation.

The thermogravimetric analysis (TGA) of the precursor gels was done on a Perkin Elmer thermal analyzer (STA-6000) at a heating rate of 10 °C min^{-1} under a N_2 atmosphere in the temperature range of 30−900 °C. The identification of the phase for the synthesized samples was carried out on a Bruker, D8-Advance X-ray diffractometer in the 2θ range of 10−100° with a scanning step of 0.02° using an X-ray source 2.2 KW Cu anode (40 kV/40 mA). The structural characterization was then done by carrying out a Rietveld refinement analysis of the XRD data using *GSAS* software. X-ray photoelectron spectroscopy (XPS) analysis of the La-doped sample was done with a Thermo Scientific NEXA surface analyzer to determine the manganese valence state in the sample.

The oxygen stoichiometry of the phases was evaluated using the iodometric titration method at room temperature. Here, 0.05 g of sample was dissolved in 100 mL of HCl (1 M)

https://doi.org/10.1021/acsomega.2c05221
ACS Omega 2023, 8, 2010−2026

solution taken in a 250 mL conical flask. This was followed by the addition of KI in excess (~3 g), resulting in the reduction of Mn^{3+} and Mn^{4+} ions to Mn^{2+} ions with the formation of the iodine. The liberated iodine was then titrated against a standardized $Na_2S_2O_3$ solution till it becomes pale yellow. The starch solution was then added until it becomes dark blue, which finally becomes colorless on further titration with $Na_2S_2O_3$ solution, indicating the end point of the reaction.

The elemental analysis and the surface morphology of the samples were done on a Carl Zeiss, Zeiss Gemini SEM field emission scanning electron microscopy, operated at 20 kV of acceleration voltage. The diffuse reflectance spectra (DRS) of the samples were carried out on a PerkinElmer UV/vis/NIR spectrometer Lambda 1050+, and the band gap energy of the phases was calculated using the obtained results.

The magnetic moment measurement of the synthesized phases with the temperature variation from 15 to 305 K at 100 Oe was carried out under both zero-field-cooled (ZFC) and field-cooled (FC) conditions, and the magnetic moment variation with an applied magnetic field of ±2 T at 15 K were recorded on a 7410 Series VSM−Lake Shore.

The effect of pH on the surface charge of the sample was studied by determining the pH of the point of zero charge (pzc) measured using the pH drift method.[35] Here, we had taken 15 mL of 4 mM NaCl solution in a 25 mL beaker and the pH of the solution was varied from 1.5 to 12 using 1 M NaOH or 1 M HCl with an increment of 0.5 and 2 from pH 1.5 to 4 and 4 onward, respectively. Next, 20 mg of the sample was added to all the beakers and left for 2 days at room temperature to allow the stabilization of the pH. The final pH of each solution was then measured, and a graph between the initial and final pH of the solution was plotted. The point of the intersection of the two curves (without catalyst and with catalyst) is the point of zero charge pH (pH_{pzc}).

The photocatalytic evaluation of the samples was done *via* carrying out photodegradation of methylene blue (MB) dye pollutant solution using a 250 W Hg lamp (λ > 400 nm) light source fixed in a UV−visible reactor chamber. In this process, 40 mg of sample in a 250 mL beaker was mixed with 100 mL of MB solution and stirred for 1 h in a dark condition to achieve the adsorption−desorption equilibrium. The pH of the reaction mixture solution was then lowered to 2 before keeping it on a magnetic stirrer and irradiated under visible light with continuous stirring to start the photo-oxidative degradation reaction. Now, ~3 mL of aliquot was drawn from the reaction mixture after each 5 min intervals and centrifuged, and its absorbance was analyzed on a UV/vis/NIR spectrometer Lambda 1050+ for the degradation.

3. RESULT AND DISCUSSION

3.1. Thermogravimetric Analysis (TGA). The plot of thermogravimetric analysis of the prepared phases, as given in Figure 1, exhibits a three-step weight loss within the studied range of temperature for all the samples. First, a ~9% decrease in weight percentage is observed from 30 to 175 °C, which may be attributed to the loss of water present in the initial reactants. The second step involves a major weight loss of ~70% from 175 to 480 °C, which could have resulted from the combustion of the metal ions, citric acid, and ethylene glycol at around 270 °C and the liberation of by-products like H_2O, CO_2, and N_2. The third step includes a small weight loss of ~4% from 480 to 670 °C, which could be related to the gradual loss of the remaining organic residue. The thermal

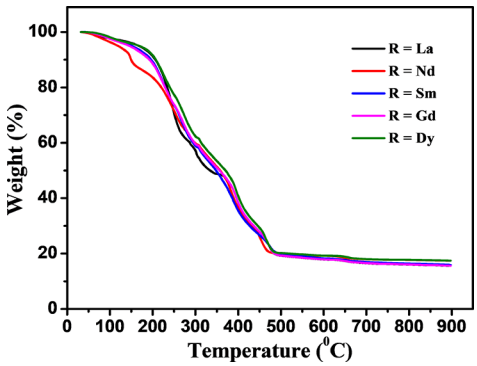

Figure 1. Thermogravimetric profile of $Sr_2La_{0.5}R_{0.5}FeMnO_7$.

decomposition above 670 °C is almost negligible as the weight loss becomes almost constant, thus indicating the formation of phases above this temperature.

3.2. Structural Analysis. The powder X-ray diffraction (PXRD) patterns of the prepared $Sr_2La_{0.5}R_{0.5}FeMnO_7$ (R = La, Nd, Sm, Gd, Dy) phases are given in Figure 2. The observed

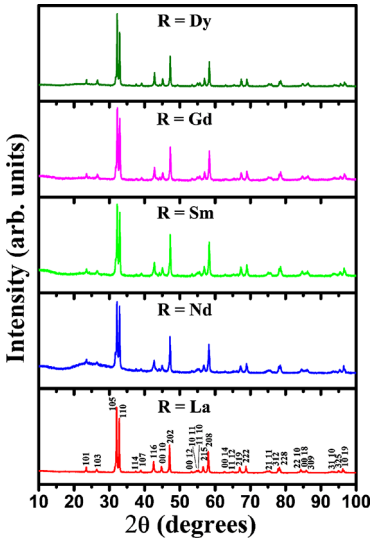

Figure 2. X-ray powder diffraction patterns of $Sr_2La_{0.5}R_{0.5}FeMnO_7$.

patterns were indexed employing the tetragonal symmetry and confirmed the phase formation for all the compounds and the absence of additional impurity. The Rietveld refinement of the PXRD data was done using the *GSAS* program[36] in the ideal tetragonal structure with the *I*4/*mmm* space group. The atomic positions were used from $Sr_3Ti_2O_7$ *n* = 2 RP oxide[37] where La/Sr(1) and La/Sr(2) were situated at 2b(0, 0, 0.5) and 4e(0, 0, *z*) positions, while Mn/Fe were at 4e(0, 0, *z*) and O(1), O(2), and O(3) were at 2a(0, 0, 0), 4e(0, 0, *z*), and 8g(0, 0.5, *z*) positions, respectively. The background zero was refined using a Chebyshev polynomial function; the peak shapes were modeled applying a pseudo-Voigt profile function; and the isothermal temperature factors (U_{iso}) were also taken. The reliable parameters resulting from the refinement analysis like the isothermal temperature factors (U_{iso}), reliability factors (R_p and R_{wp}) and the goodness of fit (χ^2) are listed in Table 1. The values of the refinement parameters (R_p, R_{wp}, and χ^2) and the observance of linearity difference between the calculated and observed diffraction patterns in the Rietveld refinement plots

https://doi.org/10.1021/acsomega.2c05221
ACS Omega 2023, 8, 2010−2026

Table 1. Structural Parameters Obtained from the Rietveld Refinement of the X-ray Diffraction Pattern for $Sr_2La_{0.5}R_{0.5}MnFeO_7$[a]

R		La	Nd	Sm	Gd	Dy
a (Å)		3.8594(1)	3.8516(1)	3.8487(1)	3.8476(1)	3.8456(1)
c (Å)		20.2441(8)	20.1691(25)	20.1428(17)	20.1085(12)	20.0810(7)
V (Å^3)		301.54(2)	299.21(4)	298.37(3)	297.69(2)	296.97(2)
z	Sr/La/R(2)	0.3148(1)	0.3146(3)	0.3149(2)	0.3147(1)	0.3152(1)
	Mn/Fe	0.1007(2)	0.1021(7)	0.1006(5)	0.0994(4)	0.0992(3)
	O(2)	0.1964(6)	0.2002(15)	0.2013(14)	0.1970(10)	0.1978(8)
	O(3)	0.0928(5)	0.0828(13)	0.0900(11)	0.0900(8)	0.0945(7)
U_{iso}(Å^2)	Sr/La/R(1)	0.01288(3)	0.01456(5)	0.01384(5)	0.01258(2)	0.01370(3)
	Sr/La/R(2)	0.01609(3)	0.01877(7)	0.01606(3)	0.01819(4)	0.01873(4)
	Mn/Fe	0.01345(5)	0.01398(6)	0.01202(2)	0.01292(2)	0.01118(5)
	O(1)	0.04664(6)	0.05092(8)	0.04206(4)	0.04793(3)	0.05360(4)
	O(2)	0.04261(2)	0.04731(7)	0.04060(3)	0.04474(2)	0.04678(5)
	O(3)	0.02290(1)	0.02533(6)	0.02180(4)	0.02732(3)	0.02637(3)
R_{wp}		0.0745	0.1015	0.0916	0.0702	0.0666
R_p		0.0571	0.0866	0.0712	0.0531	0.0504
χ^2		3.789	5.394	4.356	3.072	4.226

[a]The atomic sites are Sr/La/R(1) 2b[0, 0, 0.5]; Sr/La/R(2) 4e[0, 0, z]; Mn/Fe 4e[0, 0, z]; O(1) 2a[0, 0, 0]; O(2) 4e[0, 0, z]; O(3) 8g[0, 0.5, z] in the space group $I4/mmm$.

given in Figure 3 further affirm the formation of the synthesized phases.

The values of lattice parameters a and c and unit cell volume V obtained from structural refinements are also listed in Table 1, and their variation with the average A-site cation radius $\langle r_A \rangle$ is shown in Figure 4. It can be seen that as the value of R changes from La to Dy, the lattice constant (a & c) and the unit cell volume (V) decreases monotonically, which could be due to the decrease in the lanthanide ionic radii with the substitution.[38]

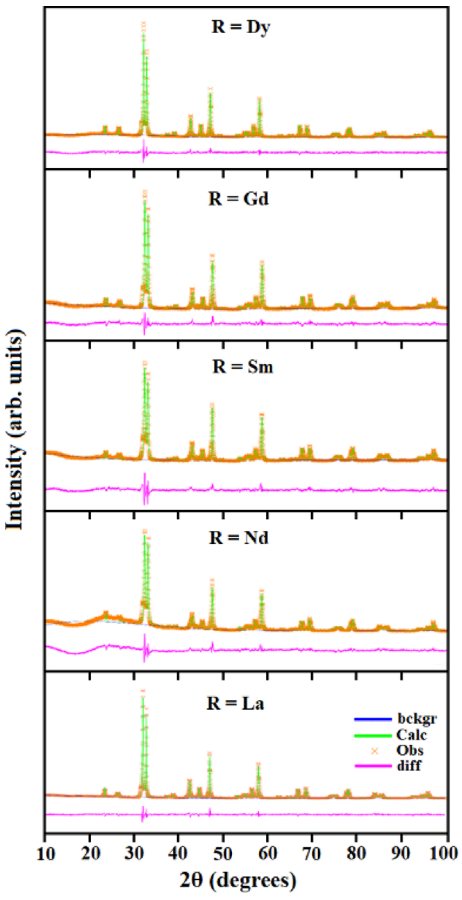

Figure 3. Rietveld refinement plots of $Sr_2La_{0.5}R_{0.5}FeMnO_7$.

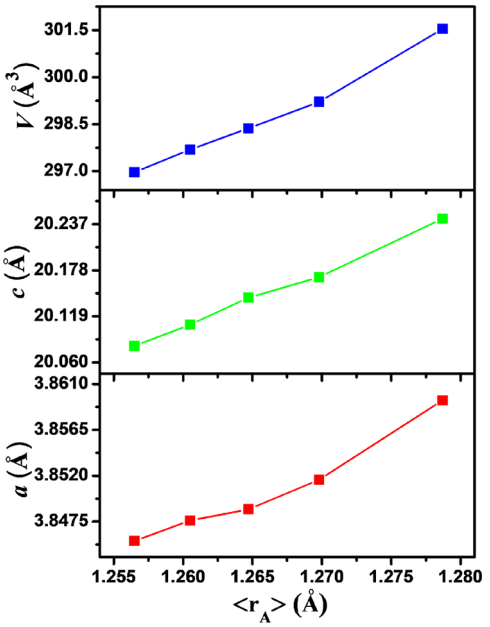

Figure 4. Variation of cell parameters and unit cell volume as a function of A-cation radius $\langle r_A \rangle$ for $Sr_2La_{0.5}R_{0.5}FeMnO_7$.

The stability of $Sr_2La_{0.5}R_{0.5}FeMnO_7$ phases can be described in terms of the tolerance factor (t) explained by Goldschmidt and Ganguly and Rao[39,40] as

$$t = \frac{[(0.5r_{La^{3+}} + 0.5r_{R^{3+}} + 2\,r_{Sr^{2+}})/3] + r_{O^{2-}}}{\sqrt{2}[\{r_{Fe^{3+}} + r_{Mn^{4+}}\}/2 + r_{O^{2-}}]}$$

The values of tolerance factor, calculated based on Shannon's ionic radii[41] as $r_{Sr^{2+}}$ = 1.31 Å, $r_{La^{3+}}$ = 1.216 Å, $r_{Nd^{3+}}$ = 1.163 Å, $r_{Sm^{3+}}$ = 1.132 Å, $r_{Gd^{3+}}$ = 1.107 Å, $r_{Dy^{3+}}$ = 1.083 Å for the coordination number 9, $r_{Mn^{4+}}$ = 0.53 Å, $r_{Fe^{3+}}$ = 0.645 Å in the high spin state for the coordination number 6, and $r_{O^{2-}}$ =

https://doi.org/10.1021/acsomega.2c05221
ACS Omega 2023, 8, 2010−2026

1.40 Å, are given in Table 2. The values obtained for all the phases lies within the tetragonal stability range of $0.88 \leq t \leq 0.99$, thus confirming the tetragonal symmetry of the prepared phases.

Table 2. Tolerance Factor (t) and Crystallite Size (D) of $Sr_2La_{0.5}R_{0.5}FeMnO_7$ Phases

R	t	D (nm)
La	0.9530	98.77
Nd	0.9499	81.03
Sm	0.9480	78.83
Gd	0.9465	65.88
Dy	0.9451	103.05

For all the phases, crystallite size (D) was calculated using the maximum intensity peak (105) observed in the PXRD data by employing Scherrer's equation[42]

$$D = \frac{K\lambda}{\beta_{sample} \cos\theta}$$

where K is a constant given by the value 0.90, λ (= 1.54 Å) is the wavelength of incident X-ray beam, β_{sample} gives the value of full width of the peak at the half maximum, and θ gives the value of diffraction angle. The values of crystallite size calculated using the above relation for all the phases are given in Table 2.

3.3. X-ray Photoelectron Spectroscopy (XPS) Analysis. The overall XPS spectrum of the $Sr_2LaFeMnO_7$ sample is given in Figure 5a, which shows that all the compositional elements are present in the synthesized phase. Figure 5b displays the Mn 2p spectra, and one can observe the appearance of two peaks located at 642.18 and 653.53 eV, which corresponds to $Mn_{3/2}$ and $Mn_{1/2}$, respectively; the asymmetry of the two peaks indicates the existence of the mixed valent Mn ions.[43] The peak fitting of the signal at 642 eV showed that $Mn_{3/2}$ could be resolved into two peaks at 641 and 643 eV, which can be attributed to Mn^{3+} and Mn^{4+}, respectively.[44,45]

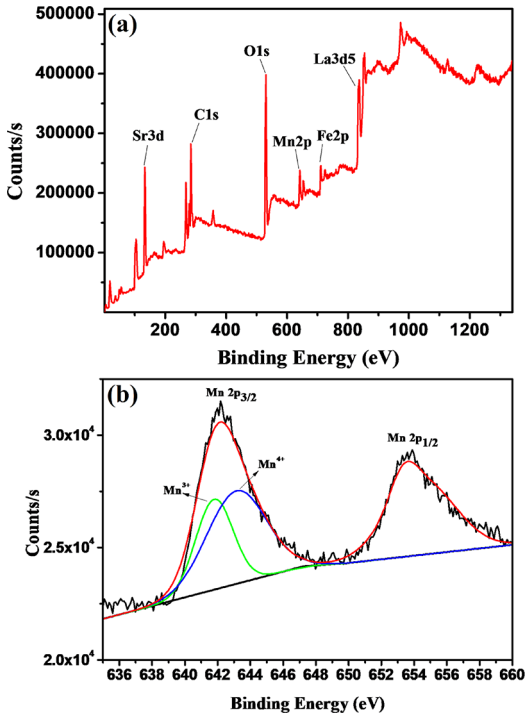

Figure 5. XPS spectrum of $Sr_2LaFeMnO_7$: (a) overall spectrum and (b) Mn 2p region.

3.4. Oxygen Stoichiometry and Elemental and Microstructural Analyses. The oxygen stoichiometry in the prepared samples was estimated from the amount of iodine liberated in the iodometric titration assuming Fe to be present in the 3+ oxidation state. The results show that the oxygen deficiency in all the phases is almost the same, and the value of oxygen content is found to be 6.96.

The elemental content of the $Sr_2La_{0.5}R_{0.5}FeMnO_7$ (R = La, Nd, Sm, Gd, Dy) phases was checked using energy dispersive X-ray (EDX) analysis, and the results are shown in Figure 6. The EDX results confirm that all the compositional elements are present in the synthesized phases, and no additional impurity is obtained during the preparation. Further, the EDX analysis results given in Table 3 indicate that there is good agreement between the theoretical elemental compositional mass percentage values and the experimental ones.

Based on the results of iodometric titrations and EDX, the formula of the phases can be written as $Sr_2La_{0.5}R_{0.5}FeMnO_{6.96}$. The stoichiometry of the phases further indicates the presence of Mn in a mixed-valence state of 3+ and 4+. The percentage content of Mn^{4+} and Mn^{3+}, calculated on the based on charge compensation, comes to be 92 and 8%, respectively. The formula of $Sr_2La_{0.5}R_{0.5}FeMnO_{6.96}$ can therefore be written as $Sr_2La_{0.5}R_{0.5}Fe(Mn^{4+}_{0.92}Mn^{3+}_{0.08})O_{6.96}$.

The crystallinity and surface morphology of the synthesized phases were done *via* FE-SEM analysis. The FE-SEM images shown in Figure 7 reveal that the $Sr_2La_{0.5}R_{0.5}FeMnO_7$ phases exhibit polycrystalline structures with irregular and spherically shaped distribution of granules. The grain sizes range in a few micrometers and show a certain extent of agglomerations. The presence of the pores in the micrographs may be related to the gases released during the high temperature sintering process.

3.5. Diffuse Reflectance Spectroscopy. The diffuse reflectance spectra (DRS) analyzed for the synthesized $Sr_2La_{0.5}R_{0.5}FeMnO_7$ (R = La, Nd, Sm, Gd, Dy) phases are shown in Figure 8. The La-doped phase is characterized by a noticeable band edge observed around 690 nm, which then shifts toward a higher wavelength with the rare earth doping in the order Nd < Sm < Dy < Gd.[46] The observed band edge could be associated with the transitions of electrons from the valence band to the conduction band.

Band gap energy (E_g) value w.r.t the obtained electronic transitions of the samples were calculated using the DRS data in the Kubelka–Munk equation[47,48]

$$F(R) = \frac{2\alpha}{S} = \frac{(1-R)^2}{2R} \quad (1)$$

where $F(R)$ denotes the Kubelka–Munk function, S is the scattering coefficient, α is the absorption coefficient, and R gives the value of absolute diffuse reflectance.

The relationship between the band gap value and the photon energy with the absorption coefficient is given by Tauc theory using the equation[49]

$$\alpha h\nu = A(h\nu - E_g)^n \quad (2)$$

https://doi.org/10.1021/acsomega.2c05221
ACS Omega 2023, 8, 2010−2026

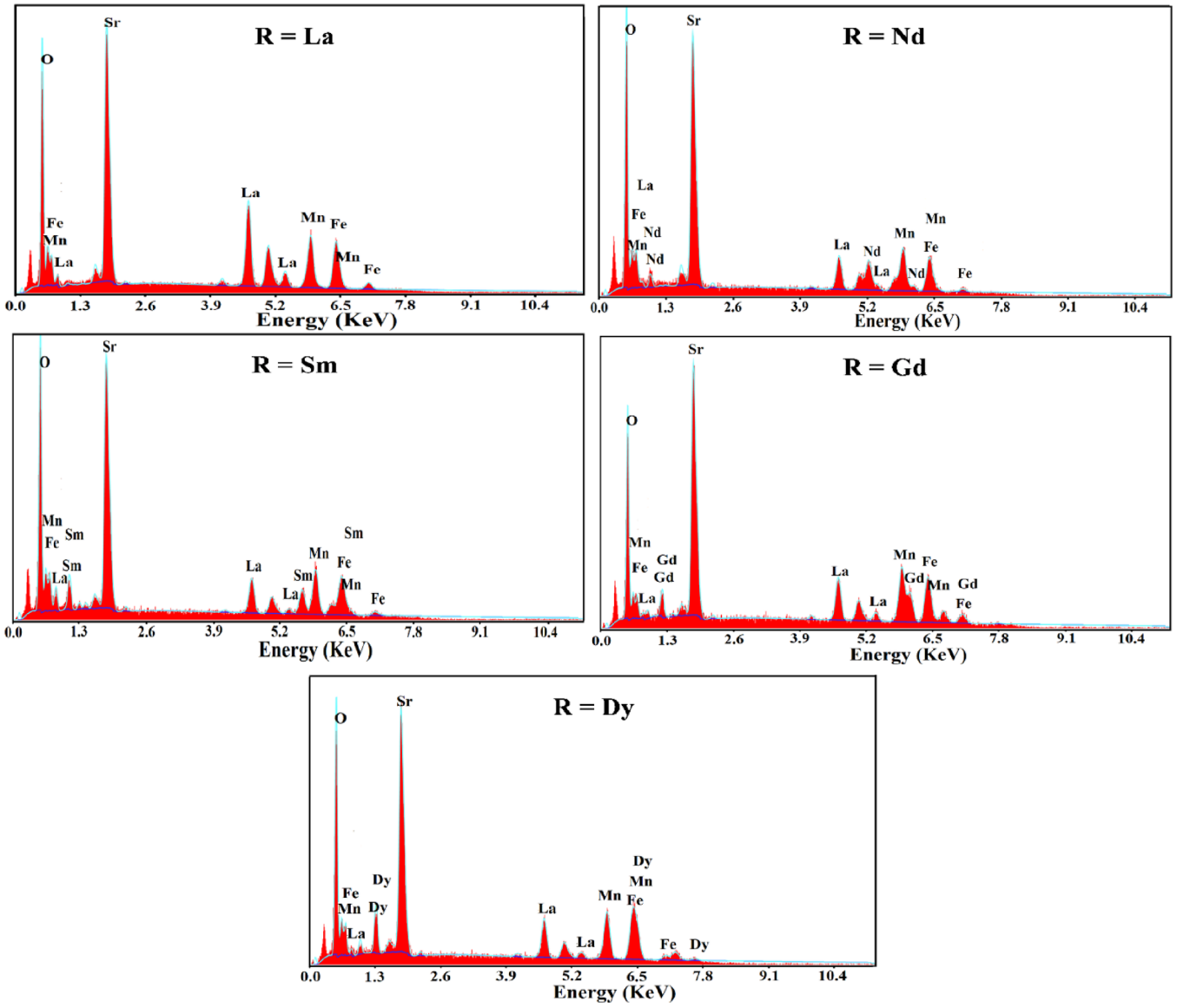

Figure 6. EDX spectra of $Sr_2La_{0.5}R_{0.5}FeMnO_7$.

Table 3. EDX Analysis of $Sr_2La_{0.5}R_{0.5}FeMnO_7$ Phases

	La		Nd		Sm		Gd		Dy	
element	expt. mass %	calc. mass %	expt. mass %	calc. mass %	expt. mass %	calc. mass %	expt. mass %	calc. mass %	expt. mass %	calc. mass%
Mn	10.14	10.23	10.04	10.17	9.91	10.12	9.93	10.06	9.83	10.01
Fe	10.26	10.40	10.21	10.35	10.20	10.29	10.15	10.23	10.01	10.18
Sr	32.60	32.64	32.35	32.48	32.2	32.29	31.92	32.09	31.82	31.94
La	25.61	25.87	12.63	12.87	12.58	12.80	12.62	12.72	12.79	12.66
R			13.20	13.37	13.80	13.86	14.23	14.40	11.4	14.81

where A is a proportionality constant, h is Planck's constant, ν the photon's frequency, and n is a constant denoting the type of electronic transition.

Using eqs 1 and 2, the Tauc relation becomes,

$$F(R)h\nu = A(h\nu - E_g)^n$$

The values of the energy band gap for the prepared phases were calculated *via* extrapolating the linear fit in the $h\nu$ vs $[F(R) \times h\nu]^2$ Tauc plot to the X-axis as displayed in Figure 9. For the La-doped sample, the band gap value was evaluated to be 1.61 eV, which is comparable to 1.6 eV for a similar type of $n = 2$ RP phase $Sr_{2.7}La_{0.3}Fe_2O_{7-\delta}$.[46] The band gap value further decreases to 1.57, 1.56, and 1.48 for Nd-, Sm-, and Gd-doped samples, respectively, and finally increases to 1.54 eV for the Dy-doped compound, indicating a narrowing of the band gap with rare earth doping, which is beneficial for the photocatalytic degradation activity.[46,50]

3.6. Magnetic Properties. The isothermal magnetization (M) dependence with the magnetic field (H) of the $Sr_2La_{0.5}R_{0.5}FeMnO_7$ system at 15 K is given in Figure 10. All the phases show a linear increase in the magnetization value with the increase in the applied magnetic field, indicating that

https://doi.org/10.1021/acsomega.2c05221
ACS Omega 2023, 8, 2010−2026

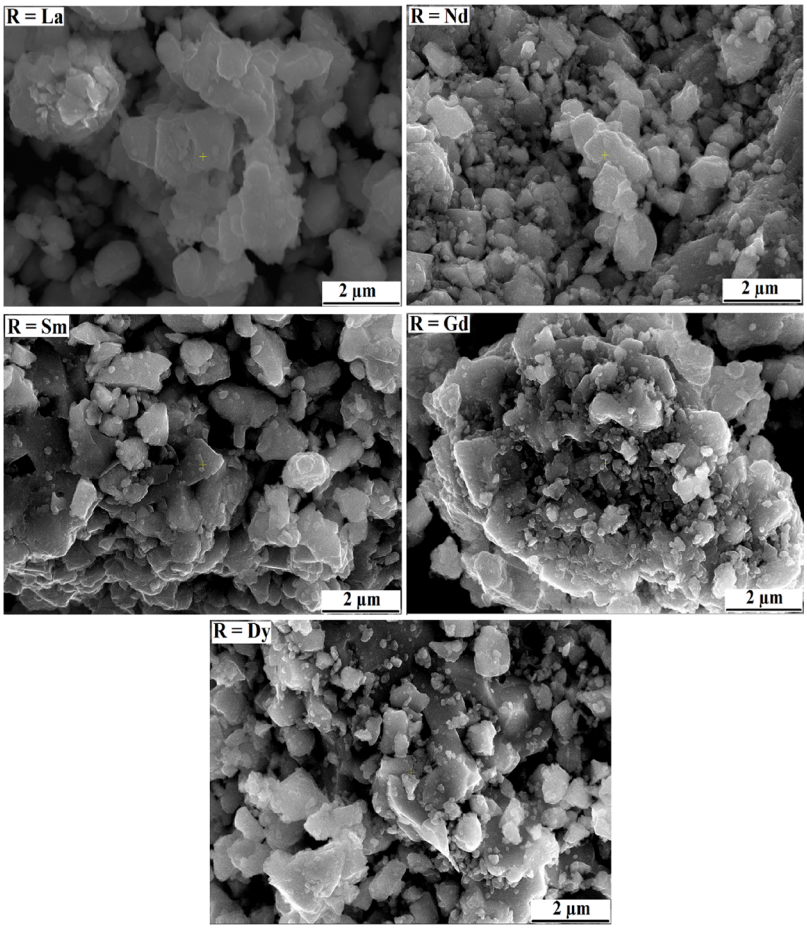

Figure 7. FE-SEM micrograph of $Sr_2La_{0.5}R_{0.5}FeMnO_7$.

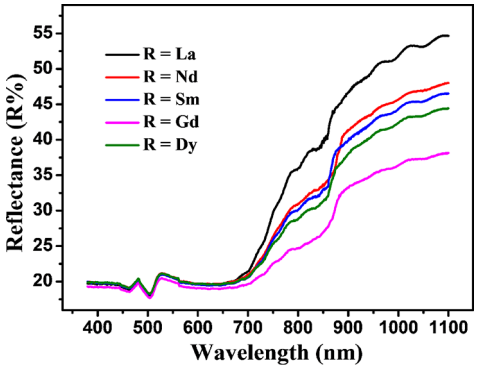

Figure 8. Diffuse reflectance spectra of the $Sr_2La_{0.5}R_{0.5}FeMnO_7$.

our samples exhibit antiferromagnetic behavior. This observed magnetic interaction is in accordance with the results obtained for $LnSr_2MnFeO_7$ reported by Singh et al.[38] However, the unsaturated hysteresis loop observed in all the cases indicates the presence of weak ferromagnetism along with the observed dominant anti-ferromagnetic interactions. The values of coercivity H_c and remanent magnetization M_r obtained for $Sr_2La_{0.5}R_{0.5}FeMnO_7$ phases are given in Table 4. The magnetic behavior of RP manganites can usually be explained on the basis of the sum of net contribution from the various exchange interaction mechanisms involved, for example, the super-exchange interaction of the Mn and Fe ions *via* O ions and double exchange interactions in the case of mixed valent Mn ions. Thus, the antiferromagnetic behavior observed in our phases could be due to the $Mn^{4+}-O-Mn^{4+}$ and $Fe^{3+}-O-Fe^{3+}$ superexchange interactions,[21,22,38] while the presence of weak ferromagnetism could be explained based on $Mn^{3+}-O-Mn^{4+}$ FM double exchange interaction. Further, the $Fe^{3+}-O-Mn^{4+}$ interaction will be AFM via the pi orbitals and FM *via* the sigma orbitals.[51−53]

The variation of DC magnetization with temperature from 10 to 300 K was carried out with a 100 Oe applied magnetic field under both zero-field-cooled (ZFC) and field-cooled (FC) conditions. The plots of molar magnetic susceptibility (χ_M) for both ZFC and FC vs temperature (T) for the $Sr_2La_{0.5}R_{0.5}FeMnO_7$ (R = La, Nd, Sm, Gd, Dy) samples are given in Figure 11. It could be seen that with the decrease in temperature, the molar magnetic susceptibility value increases for both the ZFC and FC curves. A local maximum is observed in the ZFC molar susceptibility curve at 150, 147, 138, 113, and 117 K for La-, Nd-, Sm-, Gd-, and Dy-doped samples respectively. The plot of $d\chi_M/dT$ versus T given as an inset of Figure 11 identified these maxima as their Neel temperature (T_N) owing to the 2D antiferromagnetic ordering obtained in the present phases.[21,51] The values of Neel temperature (T_N) given in Table 4 indicate that with the rare earth doping from La to Dy, the antiferromagnetic character decreases except for the Dy-doped sample. The reason could be attributed to the decrease in the average <*A*> site radius with the substitution of the heavier rare earth ion. Additionally the decrease in the average <*A*> site radius results in the tilt of $(Mn/Fe)O_6$ octahedra, which causes the reduction in the (Mn/Fe)−O−

https://doi.org/10.1021/acsomega.2c05221
ACS Omega 2023, 8, 2010−2026

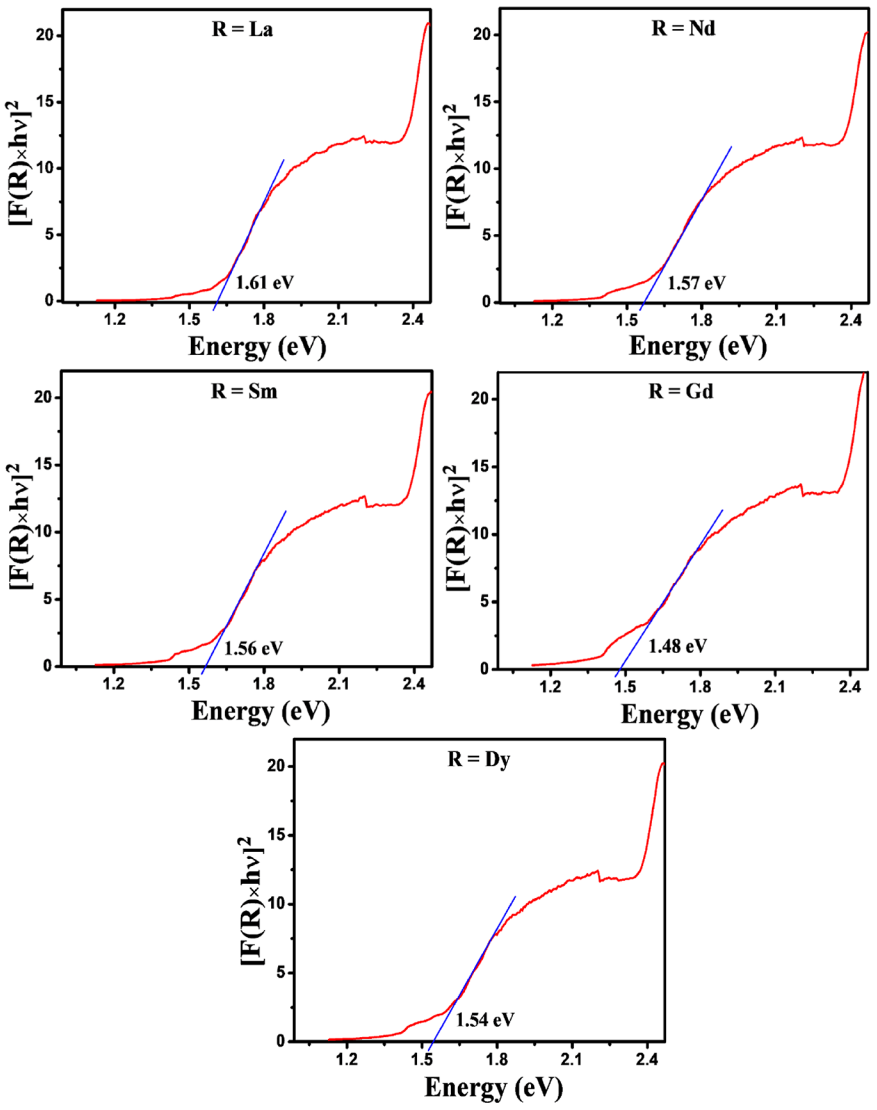

Figure 9. Tauc plot transformation of the diffuse reflectance spectra of $Sr_2La_{0.5}R_{0.5}FeMnO_7$.

(Mn/Fe) angle. As a consequence, (Mn/Fe)−O−(Mn/Fe) overlap changes that ultimately leads to a decrease in the magnitude of superexchange interactions.[38,54] The irreversibility observed between the ZFC and FC curve could have resulted from the coexistence of competing antiferromagnetic and weak ferromagnetic interactions because of the randomly substituted Mn^{4+}, Mn^{3+}, and Fe^{3+} ions at the B-site. Usually, this kind of competing magnetic interaction leads to magnetic frustrations resulting in spin glass behavior.[52,55] However, no such behavior could be observed in our phases, implying that the magnetic frustration in the present compound is not strong enough to cause a spin glass transition, but it only perturbs the spin arrangement in the samples.[56]

Figure 12 shows the plot of inverse molar magnetic susceptibility versus temperature. It can be seen that no linear region is observed within the studied temperature range, and therefore, the Curie−Weiss law will not be applicable to all our synthesized phases.

3.7. Photo-Oxidative Degradation of Dye. The photo-oxidative degradation of the methylene blue (MB) dye pollutant model was done under visible irradiation to investigate the photocatalytic activity of the $Sr_2La_{0.5}R_{0.5}FeMnO_7$ samples.

3.7.1. Control Experiments. To establish the role of the prepared samples as photocatalysts and their efficiency dependence on light and under dark conditions, the following three sets of experiments were performed using the La-doped sample: (i) dye + light, (ii) dye + catalyst + dark, and (iii) dye + catalyst + light. All these experiments were performed under acidic conditions, i.e., at pH = 2, and the changes in the degradation efficiency observed are shown in Figure 13. The results indicate that without the catalyst, the degradation percentage is only ∼8% in 60 min, showing that almost no degradation of dye has taken place without the catalyst. However, the degradation percentage becomes 79.53% in 60 min, when the reaction is done using the catalyst under dark conditions. Further, it increases to 98.13% under visible light irradiation within the same time interval, demonstrating the effect of light in the enhancement of the photo-oxidative degradation of the dye.

3.7.2. Optimization of Various Components. The optimization of parameters like pH of the reaction solution, catalyst amount, and initial dye concentration was carried out in order to maximize the efficiency of degradation toward the photo-oxidative degradation of MB dye using a La-doped catalyst under visible light irradiation.

https://doi.org/10.1021/acsomega.2c05221
ACS Omega 2023, 8, 2010−2026

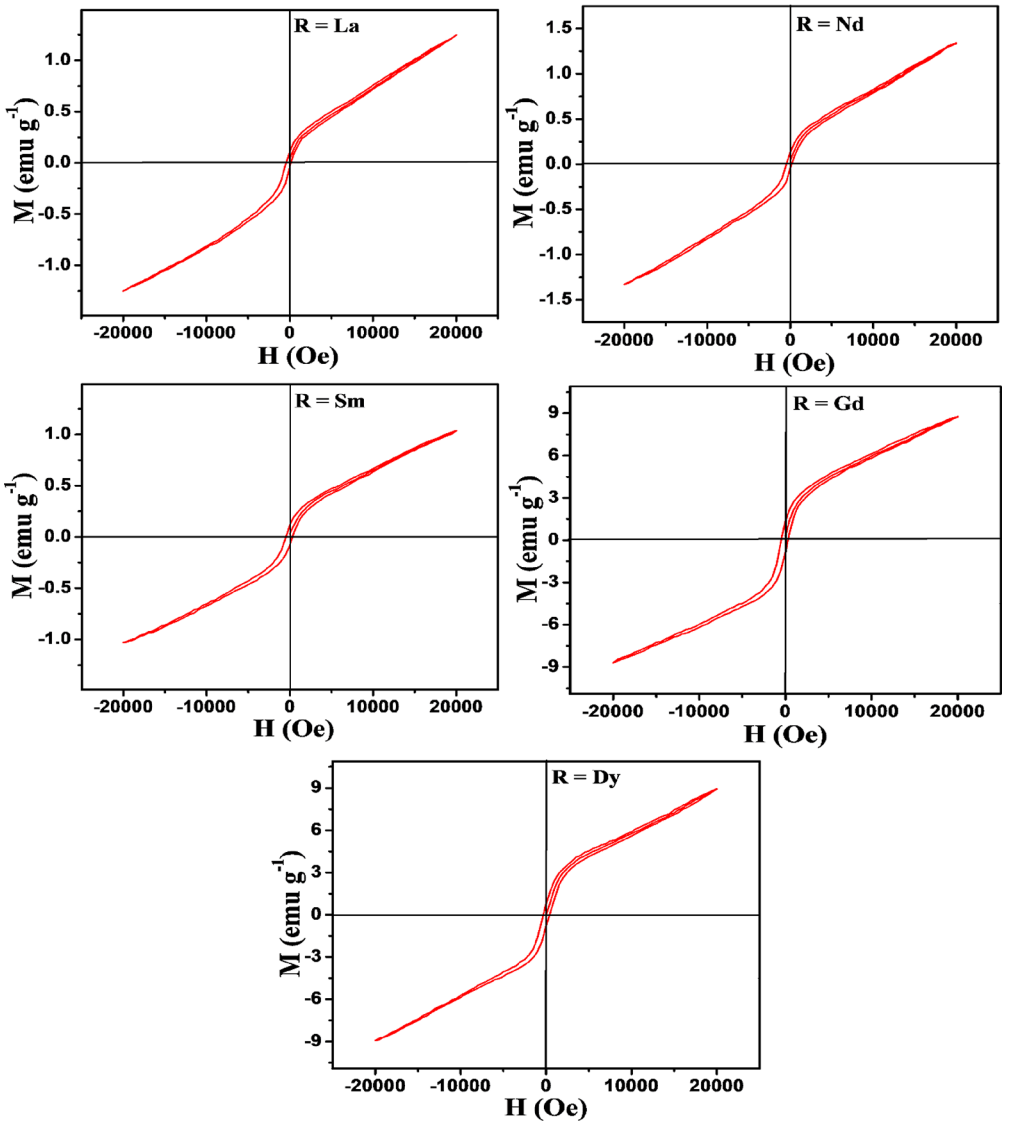

Figure 10. Variation of magnetization (M) as a function of applied magnetic field (H) for $Sr_2La_{0.5}R_{0.5}FeMnO_7$.

Table 4. Coercivity (H_c), Remanent Magnetization (M_r), and Neel Temperature (T_N) of $Sr_2La_{0.5}R_{0.5}FeMnO_7$ Phases

R	H_c (Oe)	M_r(emu g^{-1})	T_N (K)
La	294	0.107	150
Nd	329	0.128	147
Sm	372	0.131	138
Gd	408	1.348	113
Dy	383	0.759	117

3.7.2.1. Initial pH of Reaction Mixture. The optimization of the pH of the reaction mixture for achieving maximum degradation was obtained by the changing pH value from 1.5 to 3 while keeping the catalyst amount (40 mg) and MB dye concentration (8 ppm, 100 mL) the same. The results shown in Figure 14a indicate an increase in the degradation percentage from 32.12 to 64.24% and finally to 98.13% for pH = 3, 2.5, and 2, respectively, in 60 min, indicating a strong enhancement in degradation efficiency on lowering the pH value. However, on further decreasing the pH to 1.5, the degradation profile is almost similar to the one at pH = 2 and shows ~99% dye degradation in 60 min. Thus, the pH = 2 is taken as the optimized pH value and is used to carry out further photocatalytic reactions. The initial value of the pH of the reaction mixture solution plays a very important part in the dye degradation by the Mn^{3+} and Mn^{4+} redox pair. It has been reported that Mn^{3+} can only remain stable under strong acidic conditions. The Mn^{3+}/Mn^{4+} are the active ions participating in the degradation of the RhB dye by $LaMnO_3$ under strong acidic conditions.[57,58] Also, the pH_{pzc} of the $Sr_2LaFeMnO_7$ sample was determined from the plot of point of zero charge given in Figure 15, and its value comes to be 7.25, which is considered to be the net neutral charge at this pH. So, it is concluded that the surface of the catalyst would have a net positive charge below 7.25 and a net negative charge at pH greater than 7.25. Thus, the sample shows very low degradation efficiency at pH 2.5 and 3 (Figure 14a) owing to the electrostatic repulsion arising between the positively charged surface and the cationic MB dye. However, at pH 1.5 and 2, the degradation of the MB is increased. This could be due to the fact that the van der Waals interaction may dominate over electrostatic repulsion, which forces the MB dye to come in contact with the catalyst surface and thereby enables the enhanced degradation.[59]

https://doi.org/10.1021/acsomega.2c05221
ACS Omega 2023, 8, 2010−2026

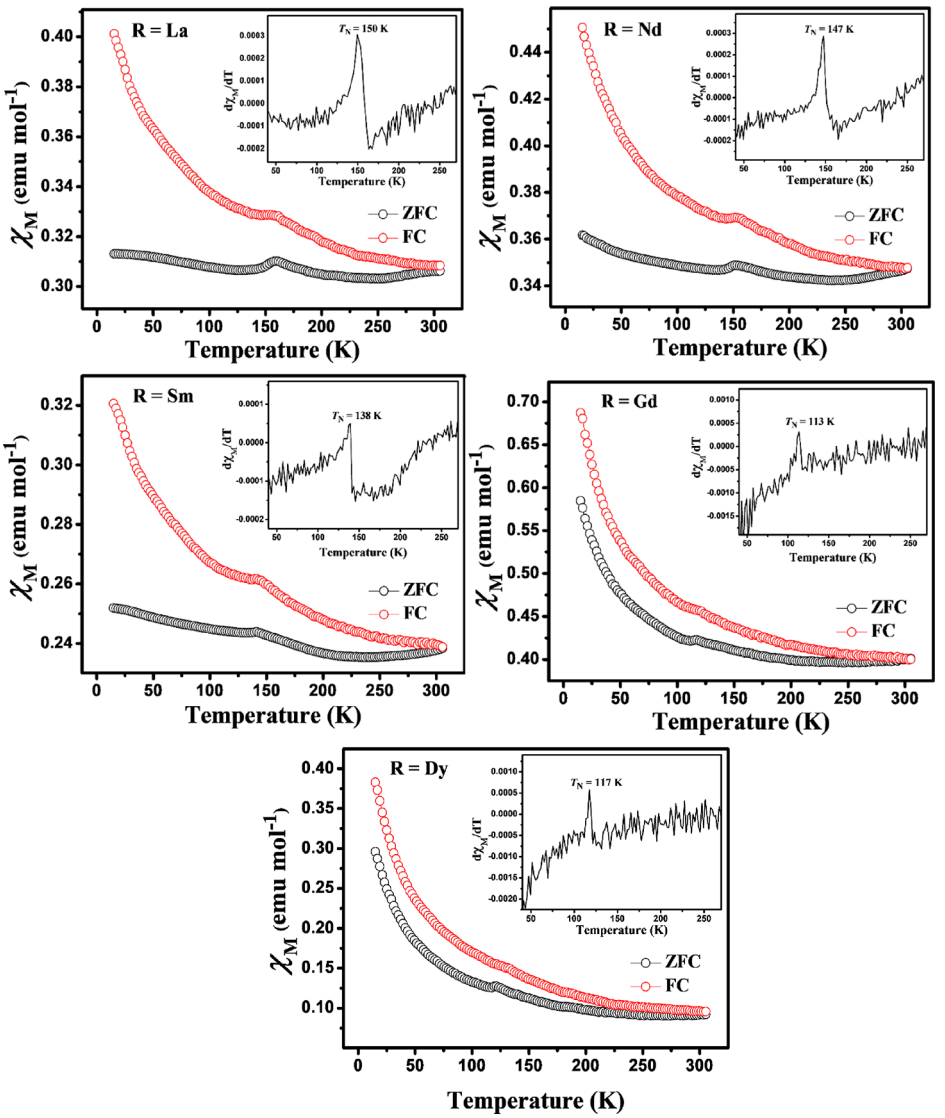

Figure 11. Plot of ZFC and FC molar magnetic susceptibility (χ_M) versus temperature of $Sr_2La_{0.5}R_{0.5}FeMnO_7$ (inset shows the $d\chi_M/dT$ vs T ZFC plot).

3.7.2.2. Catalytic Dosage. The catalyst amount for the MB dye photodegradation was changed from 20 to 50 mg to obtain the maximum degradation efficiency while keeping the pH (= 2) and MB dye concentration (8 ppm, 100 mL) the same. The catalytic dosage effect on the degradation percentage is shown in Figure 14b. The results indicate that the degradation percentage increases to 91.08, 94, and 98.13% for 20, 30, and 40 mg catalysts, respectively, in 60 min. The enhancement in the degradation efficiency on increasing the catalyst amount is quite understandable with the generalization that the number of active sites rises as the amount of catalyst is increased. So, the photocatalytic activity is enhanced. On further increasing the catalyst dosage to 50 mg, no substantial change in degradation efficiency is observed and 98.3% degradation is observed in 60 min. This could be explained by the fact that, at a certain point, increasing the catalyst amount causes the suspension of the reaction mixture to become turbid. As a result, there is a reduction in light penetration, which lowers the production of electron−hole pairs and lowers activity.[60] Thus, 40 mg of catalyst was taken as the optimized amount for carrying the reactions of dye photodegradation.

3.7.2.3. Initial Dye Concentration. The optimum concentration of the dye solution was checked by changing its value from 4 to 8 ppm while keeping the pH (= 2) and catalyst amount (40 mg) the same. Figure 14c shows the variation in the degradation efficiency with different dye concentrations. The degradation percentage increases to 98.13, 98.23, and 99.2% in 60 min on decreasing the dye concentration to 8, 6, and 4 ppm, respectively. The results indicate a uniform decrement in degradation efficiency on increasing the dye concentration. However, the changes are not substantial and the degradation profile is almost the same for all. Thus, 8 ppm concentration of MB dye solution was chosen as the optimal value for the photodegradation reactions.

3.7.3. UV−Visible Spectroscopy. The MB dye shows a maximum peak at 664 nm in its UV−visible absorbance spectrum, whose intensity upon degradation decreases using the prepared phases as catalysts and disappears upon the completion of the degradation process. The breakdown of chromophores in the dyes results in the decrease of the maximum intensity peak, and that is why the dye discoloration occurs upon the degradation. The evolution of the absorption

https://doi.org/10.1021/acsomega.2c05221
ACS Omega 2023, 8, 2010−2026

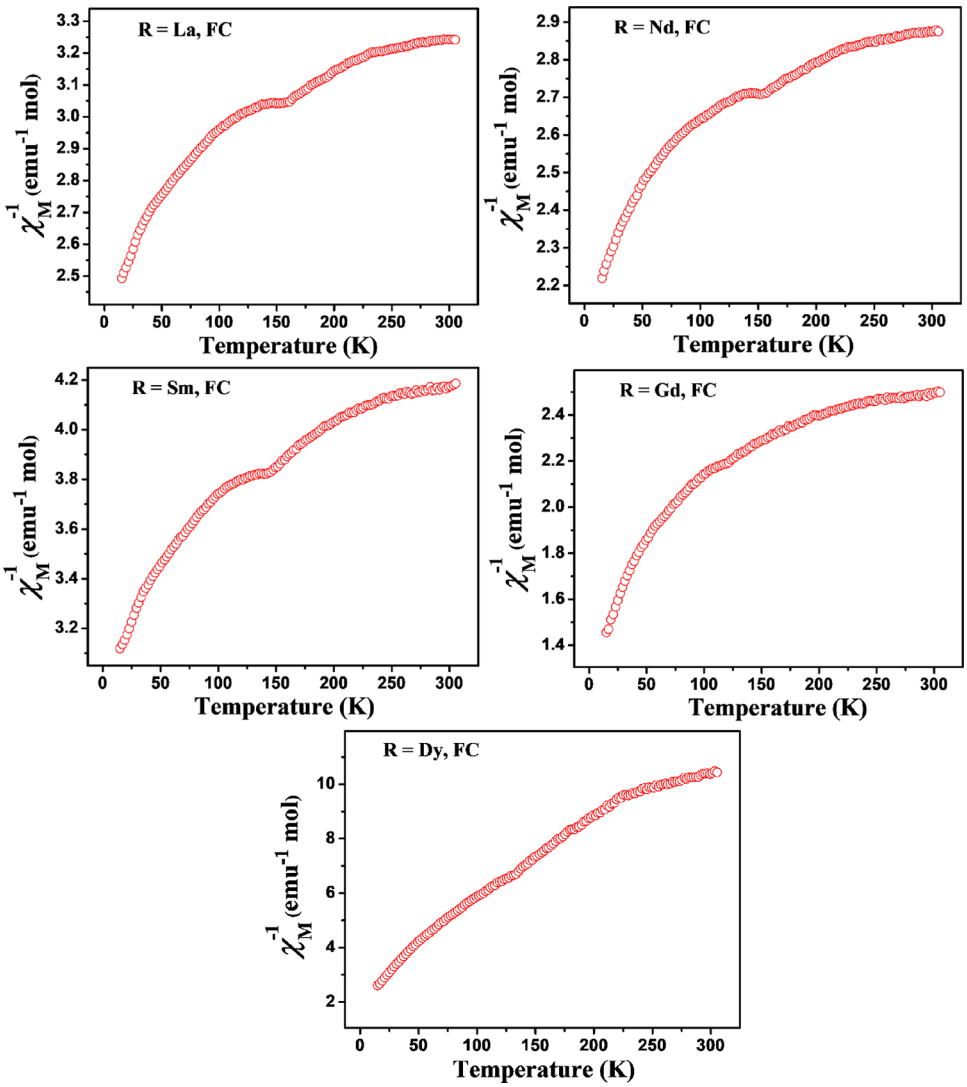

Figure 12. Plot of inverse molar magnetic susceptibility (χ_M^{-1}) versus temperature for $Sr_2La_{0.5}R_{0.5}FeMnO_7$.

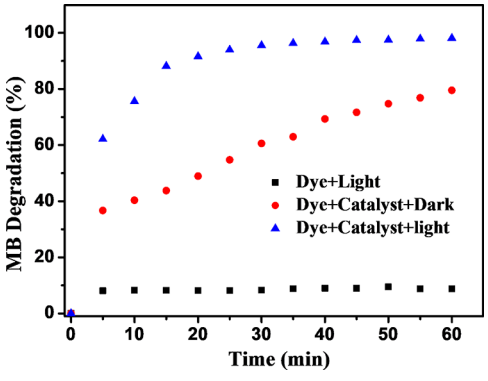

Figure 13. Time-dependent photodegradation percentage of MB without catalyst and with catalyst in dark and light conditions.

spectrum peak profile at λ = 664 nm w.r.t the time upon the photodegradation after the attainment of adsorption−desorption equilibrium is displayed in Figure 16. The degradation efficiency (DE) was further evaluated using the formula,[46]

$$\mathrm{DE}(\%) = \frac{C_o - C_t}{C_o} \times 100$$

where C_o is the initial concentration and C_t is the final concentration at time t (min).

3.7.4. Photocatalytic Mechanism for Degradation of MB Dye. As observed in the control experiments (Figure 13), the photo-oxidative degradation percentage of MB dye by the catalyst increases from 79.53 to 98.13% in 60 min when we move from dark to visible light conditions. So, the proposed catalytic mechanism followed in the MB degradation process could be seen as a combined effect of both mixed valent Mn^{3+}/Mn^{4+}redox pairs and light. The catalytic activity resulting from the Mn^{3+}/Mn^{4+} mixed valent redox pairs can be discussed as follows: it has been reported that Mn^{3+}/Mn^{4+} ions having strong reductive/oxidative properties converts O_2 molecules into active oxygen species such as O_2^-, O^{2-}, and O^-, which can then lead to the MB dye oxidative degradation.[57] The O_2 adsorbed at the catalyst surface can react with Mn^{3+} and forms a superoxide radical ion ($^{\cdot}O_2^-$) and oxidizes Mn^{3+} to Mn^{4+}. The superoxide radical thus formed reacts with the H^+ ions present in the dye solution and becomes a hydroperoxyl radical ($HO^{\cdot}_2$), which further results in the creation of hydrogen peroxide (H_2O_2). The Mn^{4+} could then react with H_2O_2 and get reduced to Mn^{3+} and produce $^{\cdot}O_2^-$. Additionally, the Fe^{3+} ion present converts Mn^{3+} to Mn^{4+} and itself reduces to Fe^{2+}.

https://doi.org/10.1021/acsomega.2c05221
ACS Omega 2023, 8, 2010−2026

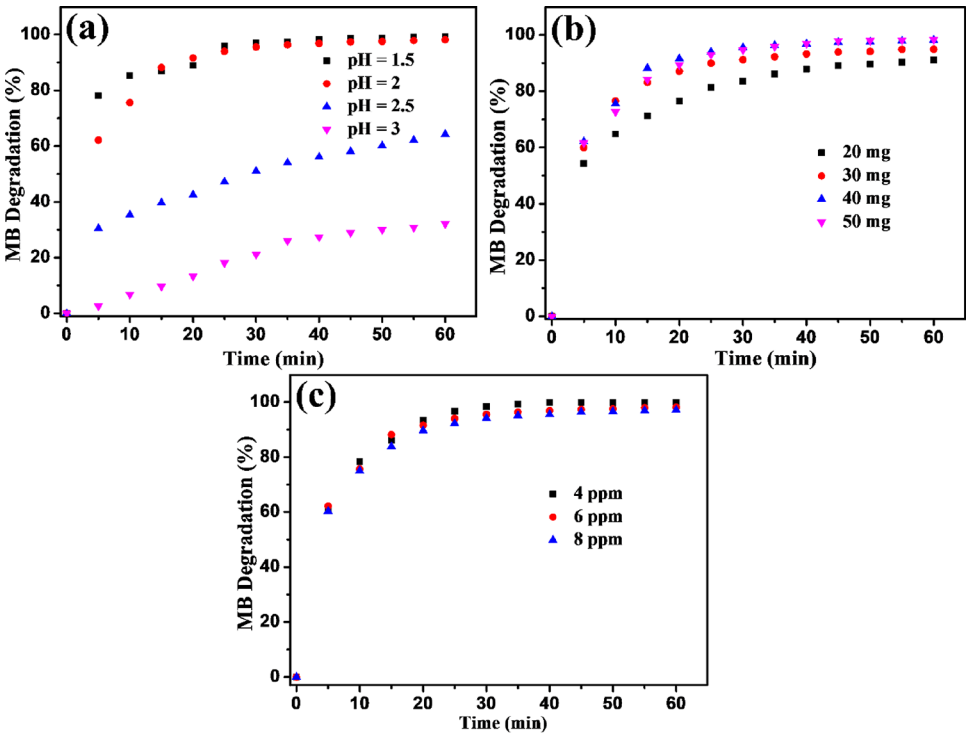

Figure 14. Dye degradation efficiency variation with (a) pH, (b) catalytic dosage, and (c) dye concentration.

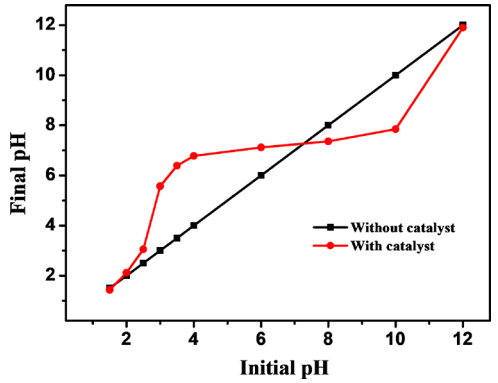

Figure 15. Plot for the determination of pH_{pzc} of La-doped catalyst.

The resulting Fe^{2+} can subsequently take part in the Fenton reaction and produces hydroxyl radicals, which will further degrade the dye pollutant.[61,62] When the reaction mixture is irradiated under visible light, the catalyst produces photo-induced electron−hole pairs and acts as powerful reducing and oxidizing agents, respectively. The water or hydroxide ions adsorbed on the surface of the catalyst react with the holes in the valence band and form a hydroxyl radical ($^{\cdot}OH$).[30,31] The $^{\cdot}OH$ being a very strong oxidizing agent will result in the degradation of the MB dye and produce various substances like water, carbon dioxide, sulfate, hydrochloric acid, and nitrate at very low concentrations. Additionally, the O_2 adsorbed on the catalyst surface reacts with the excited electrons in the conduction band and forms a superoxide radical ion ($^{\cdot}O_2^-$), which may also contribute to the degradation of the dye.[30,31] The oxygen vacancies in the synthesized phases, though small, may cause strong absorption of H_2O, O_2, and OH^- on the catalyst surface, which then can react with electron−hole pairs generated and forms active species such as $^{\cdot}OH$ and $^{\cdot}O_2^-$ radicals, further leading to the enhancement in the dye degradation.[63] The possible mechanism for the photo-degradation of MB dye can be represented as

(i) Mechanism due to the Mn^{3+}/Mn^{4+} redox pairs:

$$Mn^{3+} + O_2 \rightarrow Mn^{4+} + {}^{\cdot}O_2^-$$

$${}^{\cdot}O_2^- + H^+ \rightarrow HO_2^{\cdot}$$

$$HO_2^{\cdot} + HO_2^{\cdot} \rightarrow H_2O_2 + O_2$$

$$Mn^{4+} + H_2O_2 \rightarrow Mn^{3+} + {}^{\cdot}O_2^- + 2H^+$$

$$Mn^{3+} + Fe^{3+} \rightarrow Mn^{4+} + Fe^{2+}$$

$$Fe^{2+} + H_2O_2 \rightarrow Fe^{3+} + {}^{\cdot}OH + OH^-$$

(ii) Photocatalytic mechanism:

$$RP + h\nu \rightarrow RP(h_{VB}^+ + e_{CB}^-)$$

$$RP(h_{VB}^+) + OH^- \rightarrow RP + \cdot OH$$

$$RP(e_{CB}^-) + O_2 \rightarrow RP + {}^{\cdot}O_2^-$$

$$MB + \cdot OH + {}^{\cdot}O_2^- \rightarrow \text{degraded product} + CO_2 + H_2O + \text{others}$$

A schematic diagram illustrating the proposed mechanism is shown as Figure 17.

3.7.5. Comparison of MB Degradation with Rare Earth Doping. To assess the effect of rare earth doping on photocatalysis, the MB dye degradation was also done for other rare earth-doped catalysts under the optimized conditions and the results are displayed in Figure 18. For R = La the degradation percentage is 97.51% in 50 min, which then follows the trend, 98% for R = Nd, 98.36% for R = Sm,

https://doi.org/10.1021/acsomega.2c05221
ACS Omega 2023, 8, 2010−2026

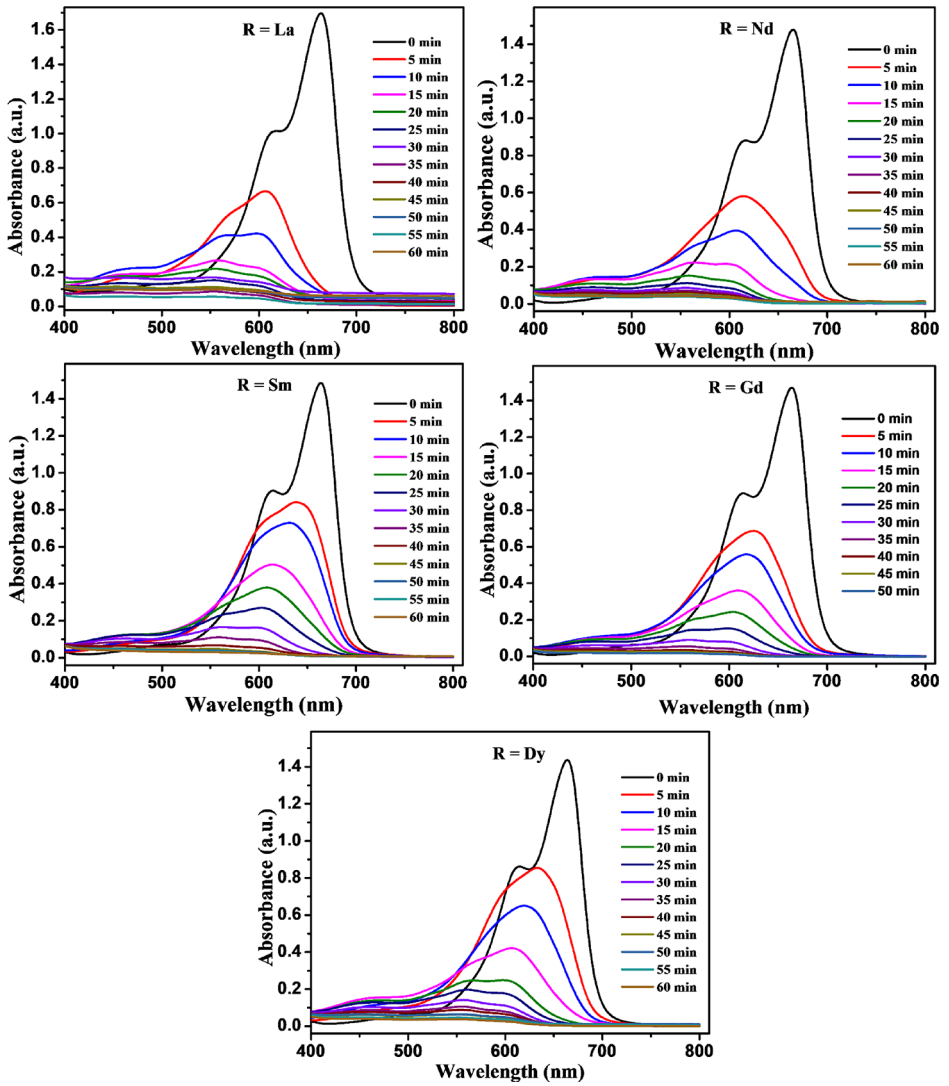

Figure 16. Time-dependent UV−vis absorbance spectrum of MB dye by the $Sr_2La_{0.5}R_{0.5}FeMnO_7$ catalyst.

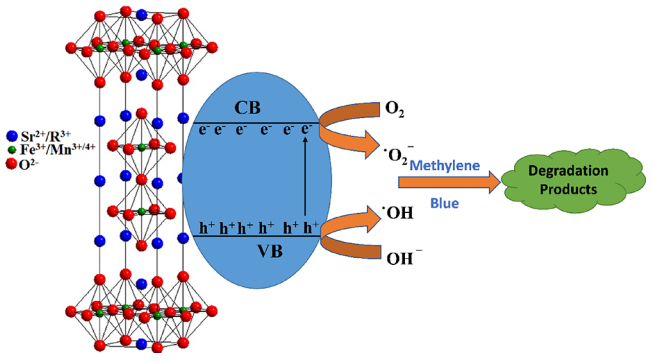

Figure 17. Schematic of MB dye degradation by $Sr_2La_{0.5}R_{0.5}FeMnO_7$ phases.

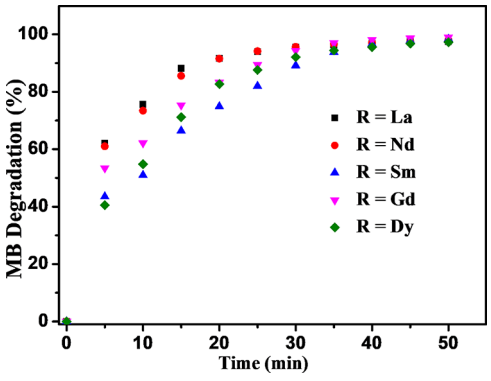

Figure 18. Time-dependent photodegradation percentage of MB dye by $Sr_2La_{0.5}R_{0.5}FeMnO_7$.

99.03% for R = Gd, and 97.26% for R = Dy samples in the same time interval. The results indicate that the photodegradation enhances with R doping till Gd and then decreases for the Dy-doped catalyst. The enhancement in photodegradation of dye was also observed when La is replaced by Nd in $Sr_{2.7}Ca_{0.3}Ln_{0.3}Fe_2O_{7-\delta}$-layered perovskite due to the lower band gap value obtained for the Nd-doped sample.[46] Song et al.[50] showed that in the case of rare earth doping in $SrTiO_3$ oxide, the maximum degradation was exhibited by the Yb-doped catalyst due to the smaller particle size and band gap, while the photocatalytic activity decreases for the Ce-doped sample owing to its larger particle size. Thus, the results observed in our system could be explained on the basis of synergistic effect of the decrease in the band gap value (Figure 9) and the crystallite size (Table 2) on R doping. The decrease

https://doi.org/10.1021/acsomega.2c05221
ACS Omega 2023, 8, 2010−2026

Table 5. Comparison of Degradation Efficiency of the Synthesized Catalysts with Reported Data

catalyst	experimental conditions	degradation %	time min	reference
$Sr_2La_{0.5}Gd_{0.5}FeMnO_7$	dose = 0.4 g L^{-1}; MB = 8 ppm; pH = 2; visible light	99.03	50	this work
Ln-doped $MgFeO_4$	dose = 0.5 g L^{-1}; MB = 10 ppm; H_2O_2–20.0 mM; pH = 6; visible light	98.9	60	[64]
$La_{0.7}Ca_{0.3}MnO_3$	dose = 0.07 g L^{-1}; MB = 7 ppm; pH = 4; visible light	73	360	[31]
$Sr_{2.4}Ca_{0.8}La_{0.8}Fe_{1.5}Co_{1.5}O_{10-\delta}$	dose = 0.3 g L^{-1}; MB = 25 ppm; pH = 6; sunlight	100	150	[33]
$Sr_{2.4}Ca_{0.3}Nd_{0.3}Fe_2O_{7-\delta}$	dose = 0.3 g L^{-1}; MB = 25 ppm; pH = 7.2; UV light	95	300	[46]
	dose = 0.3 g L^{-1}; MB = 25 ppm; pH = 7.2; sunlight	99	180	

in the band gap value facilitates the generation of more and more electron–hole pairs, while the smaller crystalloid size provides higher surface area and thus more active sites. Hence, an increase in the degradation efficiency was observed with rare earth doping. However, the smaller degradation efficiency in the case of the Dy-doped sample could be due to its larger energy band gap and crystallite size. Although limited literature is available on RP photocatalysts, a comparison of degradation efficiency with similar types of metal oxides is given in Table 5.

3.7.6. Identification of Reactive Radical Species. To determine which oxidizing agent(s) is/are more actively driving the dye degradation process, radical trapping experiments were carried out. For the detection of $^{\cdot}OH$ and $^{\cdot}O_2^-$ radicals, 2-propanol and benzoquinone were utilized as the respective radical scavengers.[46,65] The procedure follows the addition of 0.4 M 2-propanol and 0.46 mM of benzoquinone (BQ) to the already finalized reaction conditions for carrying the MB degradation as discussed earlier using the Gd-doped catalyst. The results displayed in Figure 19 show that the

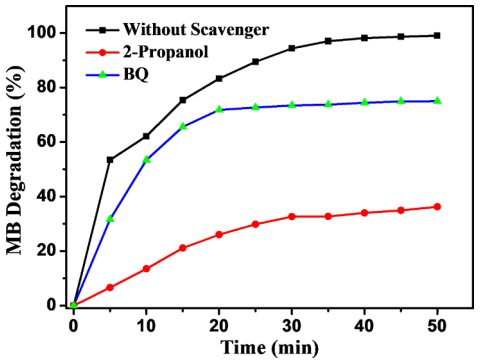

Figure 19. Effect of scavengers 2-propanol and BQ on the MB degradation percentage.

degradation of the MB dye is immensely affected with the addition of 2-propanol, achieving a degradation efficiency of 36.26% compared to 99.03% obtained without the addition of the scavengers, thus indicating the involvement of the hydroxyl radicals in the degradation process. However, with the addition of benzoquinone, the degradation efficiency decreases to 74.97%. This means that the $^{\cdot}O_2^-$ radical is making quite a lesser effect on degradation compared to the $^{\cdot}OH$ radical. Therefore, it is concluded that both $^{\cdot}O_2^-$ and $^{\cdot}OH$ radicals are responsible for the degradation of the MB dye where the $^{\cdot}OH$ radical was the main/dominant oxidizing agent involved.

3.7.7. Reusability of the Catalyst. The reusability and the stability of the synthesized phases were investigated by performing the recyclability experiment three times using the Gd-doped sample for the degradation of MB dye. After each photocatalytic test, the catalyst was centrifuged, filtered, and washed repeatedly using ethanol & distilled water and dried in an oven at 120 °C for 2 h before being reintroduced for the next experimental run. The results, as given in Figure 20, show

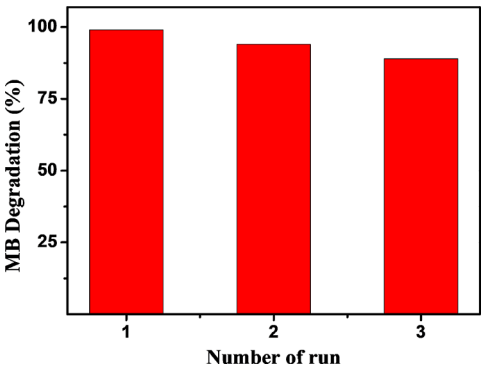

Figure 20. Reusability and stability of the $Sr_2La_{0.5}Gd_{0.5}FeMnO_7$ phase in the photocatalytic degradation of MB for three consecutive runs.

that the degradation efficiency changes to 99, 94, and 89% after each run, indicating that our catalyst demonstrated good photocatalytic activity even after the repeated runs. A small decrease in the degradation efficiency with the increase in the number of runs could be attributed to the sample lost during the filtration process. Moreover, the analysis of powder XRD and FE-SEM (Figure 21) of the recycled catalyst indicates that the structure of the catalyst is still intact and morphology

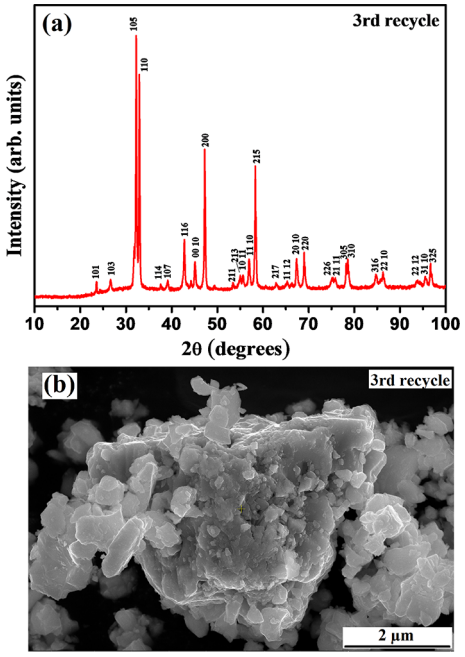

Figure 21. (a) X-ray powder diffraction patterns and (b) FESEM micrograph of $Sr_2La_{0.5}Gd_{0.5}FeMnO_7$ after the third recycle.

https://doi.org/10.1021/acsomega.2c05221
ACS Omega 2023, 8, 2010–2026

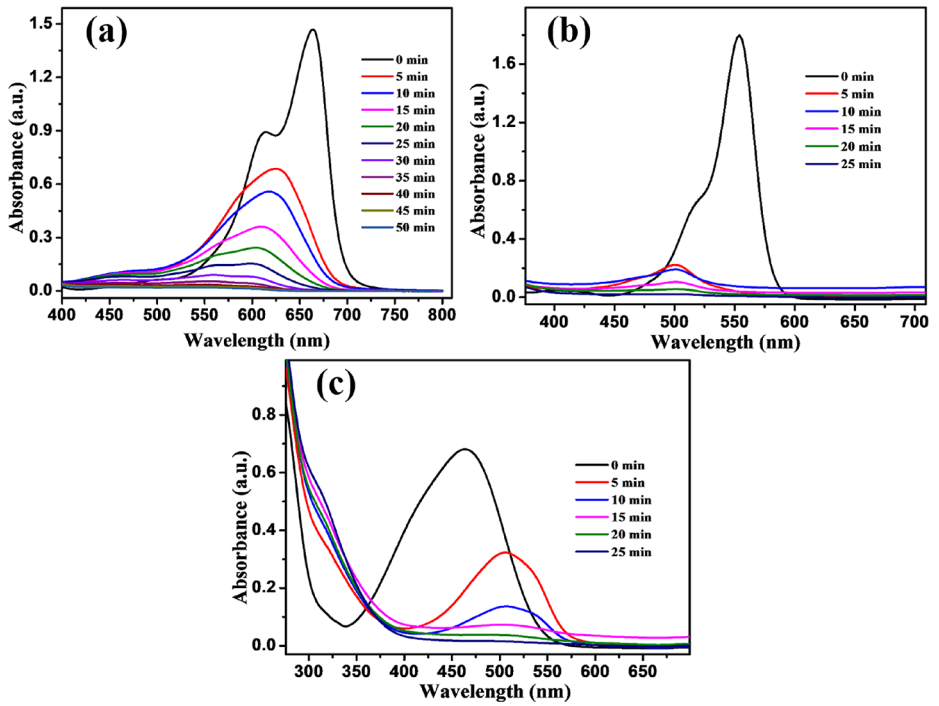

Figure 22. Time-dependent UV−vis absorbance spectrum of (a) MB (b) RhB, and (c) MO dye for $Sr_2La_{0.5}Gd_{0.5}FeMnO_7$.

almost remains the same, thus confirming their high photocatalytic stability.

3.7.8. Effectiveness of the Catalyst for the Degradation of RhB and MO Dyes. The catalyst suitability for the photodegradation of some other dye pollutants, such as rhodamine B (RhB) and methyl orange (MO) dyes, was also examined using the Gd-doped sample under the same optimal conditions as used for MB dye. The findings, as depicted in Figure 22, demonstrate that RhB and MO dyes degrade faster than MB dye, with complete degradation occurring in 25 min for both the dyes as opposed to 50 min taken for the MB dye. The obtained results may be understood in terms of the following facts: in the case of the MO dye, because of its anionic nature, it could readily attract on the catalyst surface at acidic conditions. However, due to the cationic nature of the MB dye and since the catalyst may possess a positively charged surface under acidic conditions,[66] the two may repel one another electrostatically. Therefore, MO degrades faster than the MB dye pollutant. Now, in the case of RhB dye, the faster degradation may be attributed to the negatively charged carboxylic acid group present, which could be easily attracted to the positively charged catalyst at low pH.[57]

4. CONCLUSIONS

The synthesis of $n = 2$ $Sr_2La_{0.5}R_{0.5}FeMnO_7$ RP oxides has been successfully done *via* the Sol−gel Pechini method. All the samples crystallize with the tetragonal symmetry in the *I*4/*mmm* space group. Both the unit cell parameters (a & c) and volume (V) decrease with the lanthanide substitution from La to Dy due to the decrease in their ionic radii. The results of XPS analysis and iodometric titration indicate that all the phases are oxygen deficient, and deficiency of oxygen is responsible for the Mn ions to be present in the mixed valence state of 3+ and 4+. All the phases show dominant antiferromagnetic (AFM) behavior with the appearance of weak ferromagnetic (FM) ordering. The results are explained based on net contribution from AFM Mn^{4+}−O−Mn^{4+}, Fe^{3+}−O−Fe^{3+}superexchange interactions and FM Mn^{3+}−O−Mn^{4+} double exchange interactions. The Neel temperature (T_N) decreases on the substitution of heavier rare earth ions except for the Dy-doped sample. The photo-oxidative degradation of MB dye was successfully carried out by all the prepared catalysts, and the Gd-doped sample shows the best results. The degradation efficiency increases with substitution from La to Gd, while a slight decrease is observed for the Dy-doped sample. The observed photocatalytic activity order with rare earth substitution is discussed in terms of the energy band gap and the crystallite size. The photo-oxidative degradation of other dye pollutants indicates that the RhB and MO dyes show faster degradation compared to MB dye. Since all the prepared phases show complete degradation of the dye pollutant and the recyclability experiment further confirms their high photocatalytic stability, these phases could be successfully used in wastewater treatments for environmental remediation.

AUTHOR INFORMATION

Corresponding Author

Devinder Singh − *Department of Chemistry, University of Jammu, Jammu 180006, India*; orcid.org/0000-0002-2741-302X; Email: drdssambyal@rediffmail.com

Authors

Irfan Qadir − *Department of Chemistry, University of Jammu, Jammu 180006, India*

Sumit Singh − *Department of Chemistry, University of Jammu, Jammu 180006, India*

Shikha Sharma − *Department of Chemistry, University of Jammu, Jammu 180006, India*

Ujwal Manhas − *Department of Chemistry, University of Jammu, Jammu 180006, India*

Amit Kumar Atri − *Department of Chemistry, University of Jammu, Jammu 180006, India*

https://doi.org/10.1021/acsomega.2c05221
ACS Omega 2023, 8, 2010−2026

Complete contact information is available at:
https://pubs.acs.org/10.1021/acsomega.2c05221

Notes

The authors declare no competing financial interest.

■ ACKNOWLEDGMENTS

The authors are thankful to University Grants Commission, New Delhi, India, for the financial support under JRF-178/CSIRNETJUNE2019. The authors would like to thank Director IIC IIT-Roorkee for carrying the FE-SEM studies and recording the PXRD data and Director CIF IISER-Bhopal for carrying the SQUID-VSM magnetic studies. Further, we are also thankful to the Chemistry Department, University of Jammu, for providing the instrument UV−vis−NIR spectrophotometer under RUSA 2.0.

■ REFERENCES

(1) Vasala, S.; Karppinen, M. $A_2B'B''O_6$ perovskites: a review. *Prog. Solid State Chem.* **2015**, *43*, 1−36.
(2) Kobayashi, K. I.; Kimura, T.; Sawada, H.; Terakura, K.; Tokura, Y. Room-temperature magnetoresistance in an oxide material with an ordered double-perovskite structure. *Nature* **1998**, *395*, 677−680.
(3) Filippetti, A.; Hill, N. A. Coexistence of magnetism and ferroelectricity in perovskites. *Phys. Rev. B* **2002**, *65*, No. 195120.
(4) Serrate, D.; De Teresa, J. M.; Ibarra, M. R. Double perovskites with ferromagnetism above room temperature. *J. Phys. Condens. Matter* **2007**, *19*, No. 023201.
(5) Rao, C. N. R.; Arulraj, A.; Santhosh, P. N.; Cheetham, A. K. Charge-ordering in manganates. *Chem. Mater.* **1998**, *10*, 2714−2722.
(6) Zener, C. Interaction between the d-shells in the transition metals. II. Ferromagnetic compounds of manganese with perovskite structure. *Phys. Rev.* **1951**, *82*, 403−405.
(7) Ramirez, A. P. Colossal magnetoresistance. *J. Phys. Condens. Matter* **1997**, *9*, 8171−8199.
(8) Rao, C. N. R.; Cheetham, A. K.; Mahesh, R. Giant magnetoresistance and related properties of rare-earth manganates and other oxide systems. *Chem. Mater.* **1996**, *8*, 2421−2432.
(9) Mahesh, R.; Mahendiran, R.; Raychaudhuri, A. K.; Rao, C. N. R. Effect of dimensionality on the giant magnetoresistance of the manganates: a study of the $(LaSr)_{n+1}Mn_nO_{3n+1}$ family. *J. Solid State Chem.* **1996**, *122*, 448−450.
(10) De Teresa, J. M.; Ibarra, M. R.; Garcia, J.; Blasco, J.; Ritter, C.; Algarabel, P. A.; Marquina, C.; Del Moral, A. Spin-Glass Insulator State in $(Tb\text{-}La)_{2/3}Ca_{1/3}MnO_3$ Perovskite. *Phys. Rev. Lett.* **1996**, *76*, 3392−3395.
(11) Battle, P. D.; Rosseinsky, M. J. Synthesis, structure, and magnetic properties of n = 2 Ruddlesden−Popper manganates. *Curr. Opin. Solid State Mater. Sci.* **1999**, *4*, 163−170.
(12) ScottáLaskey, N. Coupled metal-insulator and magnetic transitions in LnSr2Mn2O7 (Ln = La, Tb). *Chem. Commun.* **1996**, 767.
(13) Battle, P. D.; Cox, D. E.; Green, M. A.; Millburn, J. E.; Spring, L. E.; Radaelli, P. G.; Rosseinsky, M. J.; Vente, J. F. Antiferromagnetism, Ferromagnetism, and Phase Separation in the GMR System $Sr_{2-x}La_{1+x}Mn_2O_7$. *Chem. Mater.* **1997**, *9*, 1042−1049.
(14) Battle, P. D.; Blundell, S. J.; Green, M. A.; Hayes, W.; Honold, M.; Klehe, A. K.; Laskey, N. S.; Millburn, J. E.; Murphy, L.; Rosseinsky, M. J.; Samarin, N. A.; Singleton, J.; Sluchanko, N. E.; Sullivan, S. P.; Vente, J. F.Colossal magnetoresistance in $Sr_{2-x}Nd_{1+x}Mn_2O_7$ (x = 0.0, 0.1). 1996, *8*, L427−L434, DOI: 10.1088/0953-8984/8/32/001.
(15) Battle, P. D.; Green, M. A.; Laskey, N. S.; Millburn, J. E.; Radaelli, P. G.; Rosseinsky, M. J.; Sullivan, S. P.; Vente, J. F. Crystal and magnetic structures of the colossal magnetoresistance manganates $Sr_{2-x}Nd_{1+x}Mn_2O_7$ (x = 0.0, 0.1). *Phys. Rev. B* **1996**, *54*, 15967.
(16) Battle, P. D.; Millburn, J. E.; Rosseinsky, M. J.; Spring, L. E.; Vente, J. F.; Radaelli, P. G. Neutron diffraction study of the structural and electronic properties of $Sr_2HoMn_2O_7$ and $Sr_2YMn_2O_7$. *Chem. Mater.* **1997**, *9*, 3136.
(17) Moritomo, Y.; Maruyama, Y.; Akimoto, T.; Nakamura, A. Layered-type antiferromagnetic state in double-layered manganites: $(La_{1-z}Nd_z)_{2-2x}Sr_{1+2x}Mn_2O_7$. *J. Phys. Soc. Jpn.* **1998**, *67*, 405−408.
(18) Nair, S.; Banerjee, A. Dilution of two-dimensional antiferromagnetism by Mn site substitution in $La_1Sr_2Mn_{2-x}Al_xO_7$. *Phys. Rev. B* **2004**, *70*, No. 104428.
(19) Sharma, I. B.; Magotra, S. K.; Singh, D.; Batra, S.; Mudher, K. D. S. Synthesis, structure, electric transport and magnetic properties of $Sr_2LaMnFeO_7$ and $Sr_2LaMn_{1.5}Fe_{0.5}O_7$. *J. Solid State Chem.* **1999**, *291*, 16−20.
(20) Zhang, R. L.; Zhao, B. C.; Song, W. H.; Ma, Y. Q.; Yang, J.; Sheng, Z. G.; Dai, J. M.; Sun, Y. P. The influence of Cr doping on the charge-ordering state in bilayered $LaSr_2Mn_2O_7$. *J. Appl. Phys.* **2004**, *96*, 4965−4969.
(21) Shin, J. H.; Song, M. S.; Lee, J. Y. Structure and magnetic properties of R-P phase $Sr_3Mn_{2-x}Fe_xO_{7-\delta}$ ($0.10 \leq x \leq 0.5$). *J. Electroceram.* **2006**, *17*, 205−209.
(22) Anusree, V. K.; Das, R. R.; Lekshmi, P. N.; Dhal, R.; Colin, C. V.; Santhosh, P. N. Giant exchange bias effect in Ruddlesden-Popper oxides $SrLaFe_{0.25+x}Mn_{0.25}Co_{0.5-x}O_4$ (x = 0, 0.25): Role of the cluster glass magnetic phase in a quasi-two-dimensional perovskite. *Phys. Rev. B* **2020**, *102*, No. 134405.
(23) Jawed, A.; Kar, P.; Verma, R.; Shukla, K.; Hemanth, P.; Thakur, V. K.; Pandey, L. M.; Gupta, R. K. Integration of biological control with engineered heterojunction nano-photocatalysts for sustainable and effective management of water hyacinth weed. *J. Environ. Chem. Eng.* **2022**, *10*, No. 106976.
(24) Kar, P.; Shukla, K.; Jain, P.; Gupta, R. K. An activated carbon fiber supported Fe_2O_3@ bismuth carbonate heterojunction for enhanced visible light degradation of emerging pharmaceutical pollutants. *React. Chem. Eng.* **2021**, *6*, 2029−2041.
(25) Kar, P.; Shukla, K.; Jain, P.; Sathiyan, G.; Gupta, R. K. Semiconductor based photocatalysts for detoxification of emerging pharmaceutical pollutants from aquatic systems: A critical review. *Nano Mater. Sci.* **2021**, *3*, 25−46.
(26) Kar, P.; Jain, P.; Kumar, V.; Gupta, R. K. Interfacial engineering of Fe_2O_3@ BOC heterojunction for efficient detoxification of toxic metal and dye under visible light illumination. *J. Environ. Chem. Eng.* **2019**, *7*, No. 102843.
(27) Singh, N.; Chakraborty, R.; Gupta, R. K. Mutton bone derived hydroxyapatite supported TiO_2 nanoparticles for sustainable photocatalytic applications. *J. Environ. Chem. Eng.* **2018**, *6*, 459−467.
(28) Singh, N.; Prakash, J.; Misra, M.; Sharma, A.; Gupta, R. K. Dual functional Ta-doped electrospun TiO_2 nanofibers with enhanced photocatalysis and SERS detection for organic compounds. *ACS Appl. Mater. Interfaces* **2017**, *9*, 28495−28507.
(29) Szabo-Bardos, E.; Somogyi, K.; Toro, N.; Kiss, G.; Horvath, A. Photocatalytic decomposition of L-phenylalanine over TiO_2: Identification of intermediates and the mechanism of photodegradation. *Appl. Catal., B* **2011**, *101*, 471−478.
(30) Daud, A.; Zulfiqar, S.; Agboola, P. O.; Shakir, I.; Warsi, M. F. $DyCr_xFe_{(1-x)}O_3$ nanoparticals prepared by wet chemical technique for photocatalytic applications. *Ceram. Int.* **2020**, *46*, 26675−26681.
(31) Arabi, A.; Fazli, M.; Ehsani, M. H. Synthesis and characterization of calcium-doped lanthanum manganite nanowires as a photocatalyst for degradation of methylene blue solution under visible light irradiation. *Bull. Mater. Sci.* **2018**, *41*, 1−8.
(32) Zhang, H.; Ni, S.; Mi, Y.; Xu, X. Ruddlesden-Popper compound Sr_2TiO_4 co-doped with La and Fe for efficient photocatalytic hydrogen production. *J. Catal.* **2018**, *359*, 112−121.
(33) Oliva, J.; Garcia, C. R.; Verduzco, E.; Martinez, A. I.; Manthiram, A.; Padmasree, K. P. Enhancing the photocatalytic activity of the perovskite-based intergrowth oxide $Sr_{3.2}La_{0.8}Fe_{1.5}Co_{1.5}O_{10-\delta}$ with Ca substitution. *Ceram. Int.* **2017**, *43*, 14074−14081.

(34) Guo, J.; Jing, Y.; Shen, T.; Luo, H.; Liang, J.; Yuan, S. Effect of doped strontium on catalytic properties of $La_{1-x}Sr_xMnO_3$ for rhodamine B degradation. *J. Rare Earths* **2021**, *39*, 1362−1369.
(35) Bishnoi, S.; Kumar, A.; Selvaraj, R. Facile synthesis of magnetic iron oxide nanoparticles using inedible Cynometra ramiflora fruit extract waste and their photocatalytic degradation of methylene blue dye. *Mater. Res. Bull.* **2018**, *97*, 121−127.
(36) Larson, A. C.; Von Dreele, R. B.*Report LAUR*; Los Alamos National Laboratory:New Mexico, USA2000, 86−748.
(37) Ruddlesden, S. N.; Popper, P. The compound $Sr_3Ti_2O_7$ and its structure. *Acta Crystallogr.* **1958**, *11*, 54−55.
(38) Singh, D.; Sharma, S.; Mahajan, A.; Singh, S.; Singh, R. Synthesis and characterization of layered perovskite-type oxides $LnSr_2MnFeO_7$ (Ln = La, Nd, Gd, and Dy). *Ionics* **2013**, *19*, 19.
(39) Goldschmidt, V. M.*Mat.-Naturv. Kl*Skrifer Norske Videnskaps-Akad: Oslo, I. 1926, 8.
(40) Ganguly, P.; Rao, C. N. R. Crystal chemistry and magnetic properties of layered metal oxides possessing the K_2NiF_4 or related structures. *J. Solid State Chem.* **1984**, *53*, 193−216.
(41) Shannon, R. D. Revised effective ionic radii and systematic studies of interatomic distances in halides and chalcogenides. *Acta crystallogr. Sect. A: Cryst. Phys. Diffr. Theor. Gen. crystallogr.* **1976**, *32*, 751−767.
(42) Klug, H. P.; Alexander, L. E.*X-ray diffraction procedures; for polycrystalline and amorphous materials*; John Wiley and Sons Inc: Canada1954.
(43) Niu, J.; Deng, J.; Liu, W.; Zhang, L.; Wang, G.; Dai, H.; He, H.; Zi, X. Nanosized perovskite-type oxides $La_{1-x}Sr_xMO_{3-\delta}$ (M = Co, Mn; x = 0, 0.4) for the catalytic removal of ethylacetate. *Catal. Today* **2007**, *126*, 420−429.
(44) Zhou, D.; Li, J.; Chen, C.; Lin, F.; Wu, H.; Guo, J. A hydrothermal synthesis of Ru-doped $LiMn_{1.5}Ni_{0.5}O_4$ cathode materials for enhanced electrochemical performance. *RSC Adv.* **2021**, *11*, 12549−12558.
(45) Hu, J.; Wang, L.; Shi, L.; Huang, H. Oxygen reduction reaction activity of $LaMn_{1-x}Co_xO_3$-graphene nanocomposite for zinc-air battery. *Electrochim. Acta* **2015**, *161*, 115−123.
(46) Verduzco, L. E.; Garcia-Diaz, R.; Oliva, J.; Martinez, A. I.; Gomez-Solis, C.; Garcia, C. R.; Fuentes, A. F.; Padmasree, K. P. Enhanced photocatalytic activity of layered perovskite oxides $Sr_{2.7-x}Ca_xLn_{0.3}Fe_2O_{7-\delta}$ for MB degradation. *Ceram. Int.* **2018**, *44*, 17079−17086.
(47) Hussen, M. K.; Dejene, F. B.; Gonfa, G. G. Effect of citric acid on material properties of $ZnGa_2O_4$:Cr^{3+}nanopowder prepared by sol−gel method. *Appl. Phys. A: Mater. Sci. Process.* **2018**, *124*, 1−10.
(48) Morales, A. E.; Mora, E. S.; Pal, U. Use of diffuse reflectance spectroscopy for optical characterization of un-supported nanostructures. *Rev. Mex. Fis.* **2007**, *53*, 18−22.
(49) Singh, S.; Sharma, S.; Manhas, U.; Qadir, I.; Atri, A. K.; Singh, D. Different Fuel-Adopted Combustion Syntheses of Nano-Structured NiCrFeO4: A Highly Recyclable and Versatile Catalyst for Reduction of Nitroarenes at Room Temperature and Photocatalytic Degradation of Various Organic Dyes in Unitary and Ternary Solutions. *ACS Omega* **2022**, *7*, 19853−19871.
(50) Song, Y. X.; Ma, W. Q.; Chen, J. J.; Xu, J.; Mao, Z. Y.; Wang, D. J. Photocatalytic activity of perovskite $SrTiO_3$ catalysts doped with variable rare earth ions. *Rare Met.* **2021**, *40*, 1077−1085.
(51) Battle, P. D.; Branford, W. R.; Mihut, A.; Rosseinsky, M. J.; Singleton, J.; Sloan, J.; Spring, L. E.; Vente, J. F. Structural chemistry and electronic properties of the n = 3 Ruddlesden-Popper phases $Ca_4Mn_2FeO_{9.75}$ and $Sr_4Mn_2FeO_{9.80}$. *Chem. Mater.* **1999**, *11*, 674−683.
(52) Fawcett, I. D.; Veith, G. M.; Greenblatt, M.; Croft, M.; Nowik, I. Properties of the n = 3 Ruddlesden-Popper phases $Sr_4Mn_{3-x}Fe_xO_{10-\delta}$ (x = 1, 1.5, 2). *J. Solid State Chem.* **2000**, *155*, 96−104.
(53) Das, R. R.; Lekshmi, P. N.; Das, S. C.; Santhosh, P. N. Competing short-range magnetic correlations, metamagnetic behavior and spin-phonon coupling in Nd_2CoMnO_6 double perovskite. *J. Alloys Compd.* **2019**, *773*, 770−777.
(54) Sharma, I. B.; Singh, D.; Magotra, S. K. Effect of substitution of magnetic rare earths for La on the structure, electric transport and magnetic properties of $La_2SrFe_2O_7$. *J. Alloys Compd.* **1998**, *269*, 13−16.
(55) Das, R. R.; Lekshmi, P. N.; Dhal, R.; Colin, C. V.; Santhosh, P. N. Giant exchange bias effect in Ruddlesden-Popper oxides $SrLaFe_{0.25+x}Mn_{0.25}Co_{0.5-x}O_4$ (x = 0, 0.25): Role of the cluster glass magnetic phase in a quasi-two-dimensional perovskite. *Phys. Rev. B* **2020**, *102*, No. 134405.
(56) Qadir, I.; Atri, A. K.; Singh, S.; Sharma, S.; Manhas, U.; Singh, D. Synthesis of Ruddlesden-Popper $LaSrFe_{1-x}Cr_xO_4$ phases (x = 0.0, 0.2, 0.4, 0.6) by glycine-nitrate combustion process: Effect of Cr doping on magnetic, optical and photocatalytic properties. *J. Alloys Compd.* **2022**, *920*, No. 165865.
(57) Luo, H.; Guo, J.; Shen, T.; Zhou, H.; Liang, J.; Yuan, S. Study on the catalytic performance of $LaMnO_3$ for the RhB degradation. *J. Taiwan Inst. Chem. Eng.* **2020**, *109*, 15−25.
(58) Gao, Y.; Jiang, J.; Zhou, Y.; Pang, S. Y.; Ma, J.; Jiang, C.; Wang, Z.; Wang, P. X.; Wang, L. H.; Li, J. Unrecognized role of bisulfite as Mn (III) stabilizing agent in activating permanganate (Mn (VII)) for enhanced degradation of organic contaminants. *Chem. Eng. J.* **2017**, *327*, 418−422.
(59) Ridzuan, N. D. M.; Kaus, N. H. M.; Lazim, M. A. S. M.; Kobayashi, T.; Adnan, R.; Othman, M. Z.; Kassim, M. H. M. Photocatalytic heterostructures-based $BiFeO_3$ embedded liquid natural rubber (LNR) for highly removal of cationic dye under direct sunlight. *J. Environ. Chem. Eng.* **2020**, *8*, No. 104152.
(60) Gupta, N. K.; Ghaffari, Y.; Kim, S.; Bae, J.; Kim, K. S.; Saifuddin, M. Photocatalytic degradation of organic pollutants over MFe_2O_4 (M = Co, Ni, Cu, Zn) nanoparticles at neutral pH. *Sci. Rep.* **2020**, *10*, 1−11.
(61) Dai, D.; Liang, H.; He, D.; Potgieter, H.; Li, M. Mn-doped Fe_2O_3/diatomite granular composite as an efficient Fenton catalyst for rapid degradation of an organic dye in solution. *J. Sol-Gel Sci. Technol.* **2021**, *97*, 329−339.
(62) Chiam, S. L.; Pung, S. Y.; Yeoh, F. Y.; Ahmadipour, M. Highly efficient oxidative degradation of organic dyes by manganese dioxide nanoflowers. *Mater. Chem. Phys.* **2022**, *280*, No. 125848.
(63) Wei, Z. X.; Xiao, C. M.; Zeng, W. W.; Liu, J. P. Magnetic properties and photocatalytic activity of $La_{0.8}Ba_{0.2}Fe_{0.9}Mn_{0.1}O_{3-\delta}$ and $LaFe_{0.9}Mn_{0.1}O_{3-\delta}$. *J. Mol. Catal. A: Chem.* **2013**, *370*, 35−43.
(64) Ivanets, A.; Prozorovich, V.; Sarkisov, V.; Roshchina, M.; Grigoraviciute-Puroniene, I.; Zarkov, A.; Kareiva, A.; Masindi, V.; Wang, C.; Srivastava, V.; Sillanpää, M. Effect of magnesium ferrite doping with lanthanide ions on dark-, visible-and UV-driven methylene blue degradation on heterogeneous Fenton-like catalysts. *Ceram. Int.* **2021**, *47*, 29786−29794.
(65) Weldegebrieal, G. K.; Sibhatu, A. K. Photocatalytic activity of biosynthesized α-Fe_2O_3 nanoparticles for the degradation of methylene blue and methyl orange dyes. *Optik* **2021**, *241*, No. 167226.
(66) Shimizu, N.; Ogino, C.; Dadjour, M. F.; Murata, T. Sonocatalytic degradation of methylene blue with TiO_2 pellets in water. *Ultrason. Sonochem.* **2007**, *14*, 184−190.

https://doi.org/10.1021/acsomega.2c05221
ACS Omega 2023, 8, 2010−2026